Quaternary Geochronology 66 (2021) 101212

Contents lists available at ScienceDirect

Quaternary Geochronology

journal homepage: www.elsevier.com/locate/quageo

Research paper

Rock surface IRSL dating of buried cobbles from an alpine dry-stone structure in Val di Sole, Italy

Lucas Ageby [a,*], Diego E. Angelucci [b], Dominik Brill [a], Francesco Carrer [c], Eike F. Rades [d,e], Janet Rethemeyer [f], Helmut Brückner [a], Nicole Klasen [a]

[a] Institute of Geography, University of Cologne, 50923 Cologne, Germany
[b] Dipartimento di Lettere e Filosofia, University of Trento, 38122 Trento, Italy
[c] School of History, Classics and Archaeology, Newcastle University, NE1 7RU Newcastle, UK
[d] Nordic Laboratory for Luminescence Dating, Department of Geoscience, Aarhus University, Risø Campus, Roskilde, DK, 4000, Denmark
[e] Radiation Physics Section, Department of Physics, Technical University of Denmark, DTU Risø Campus, Roskilde, DK, 4000, Denmark
[f] Institute of Geology and Mineralogy, University of Cologne, 50923 Cologne, Germany

ARTICLE INFO

Keywords:
Rock surface luminescence dating
Luminescence-depth profiles
IRSL
Dry-stone structures
Val di Sole
Pastoralism

ABSTRACT

Here, we investigate the application of rock surface IRSL dating to chronology restrain archaeological structures related to upland pastoralism. We applied the method to cobbles collected from archaeological units in an excavation of a dry-stone structure in Val di Sole in the Italian Alps. At this site, archaeological finds and previous radiocarbon analyses have dated an initial human occupation of the site to the Early Bronze Age (ca. 2200–1600 BC), and a possible second occupation to the Middle Bronze Age (ca. 1600–1350 BC). These archaeological units have later been buried by colluvial sediments. Theoretically, the luminescence-depth profiles from rock surfaces from inside such structures could record the exposure and burial of these archaeological units. We collected buried gneiss cobbles from these archaeological units and measured rock slices and chips from 1 to 4 cm long cores with a low-temperature pIR-IRSL protocol to investigate the signal resetting in these cobbles. Only the $IRSL_{50}$ signal was deemed appropriate for dating. Measured luminescence-depth profiles demonstrate varying levels of signal resetting before burial. Dating of two paragneiss cobbles from the lower unit yielded corrected burial ages of ∽1450-700 BC and ∽19 ka. The older date is clearly not associated with human occupation; the younger date slightly underestimates the Early Bronze Age occupation, which was confirmed by new radiocarbon dating of charcoal (1731-1452 and 2124-1773 cal. BC). The burial of the upper archaeological unit was dated to ∽AD 1000, based on ages derived from the bottom surface of an orthogneiss cobble and the top surface of a paragneiss cobble. This is slightly younger than two new radiocarbon ages (426-596 and 537-654 cal. AD) from charcoal fragments sampled from the same unit. This new chronological data show longer exposure of the upper archaeological unit than was previously known. Furthermore, the paragneiss cobble from the upper unit has been exposed to sufficient heat to reset the $IRSL_{50}$ and $pIR\text{-}IRSL_{290}$ signals throughout the cobble; an event which can be dated to ∽AD 100–1500 BC. Comparisons between fading-corrected $IRSL_{50}$ ages and $pIR\text{-}IRSL_{290}$ ages from the heated cobble are in agreement, which suggests that the conventional g-value approach accurately corrects for signal loss during burial. Overall, our research suggests that rock surface IRSL dating can provide complementary chronological data for archaeological settings.

1. Introduction

The timing and strategies of prehistoric upland pastoralism in the European Alps remain largely uncertain. Although high-mountain pastures in the Alpine regions have historically had significant economic importance, known archaeological sites are still scarce (Carrer, 2012). Therefore, a thorough chronological understanding of site formation and periods of human impact on the environment from currently known sites is essential to infer the nature of human occupation of upland areas in the past.

Soon after the last deglaciation, groups of late Upper Paleolithic and, later, Mesolithic hunter-gatherers started to exploit high altitude (>2000 m above sea level) areas in the Alps, presumably during the summers (Cavulli et al., 2011). Lithic assemblages and scat-

* Corresponding author.
E-mail address: lageby@uni-koeln.de (L. Ageby).

https://doi.org/10.1016/j.quageo.2021.101212
Received 23 December 2020; Received in revised form 30 April 2021; Accepted 6 June 2021
Available online 10 June 2021

tered finds which indicate upland hunting during the early Holocene have been recorded from several Alpine sectors, e.g., from the eastern Southern Alps (Cavulli et al., 2011), from the Silvretta Alps (Switzerland/Austria), dated to the mid-9th millennium BC (Kothieringer et al., 2015), and slightly later (8000–7000 BC) from the French Alps (Walsh et al. 2014). Palaeoecological and archaeological records (e.g., Hafner and Schwörer, 2018; Kothieringer et al., 2015) show that intense human land use, including grazing and forest clearing, may have locally occurred during the Neolithic and the Chalcolithic, while similar studies in other sectors of the Alps (e.g., Festi et al., 2014; Walsh et al., 2007) show a modest human impact on the upland environment in these early phases. During the Bronze Age (∽2300–800 BC), grazing of upland pastures in the Alps became more established and widespread (Festi et al., 2014; Leveau and Walsh, 2005; Moe et al., 2007; Walsh et al., 2007). The oldest dry-stone structures (huts and enclosures) in the Alpine uplands date to this period, documenting a more intensive use of summer pastures (Angelucci et al., 2014; Reitmaier et al., 2018; Walsh and Mocci, 2011; Walsh et al., 2014), and possibly a transition toward more specialised dairy practices (Carrer et al., 2016).

Radiocarbon dating is the most frequently applied dating method for such structures (e.g., Angelucci et al., 2017), whereby, as a rule, the stratigraphically associated units are dated. Although radiocarbon dating is a well-established method that can provide reliable and high-precision ages, caution is advisable when choosing material for dating. Suitable materials such as wood, charcoal, and macrofossils are not always present in archaeological deposits. Furthermore, the stratigraphic relationship between sample depth and age is not always straightforward, e.g., due to the shallowness of upland soils (Angelucci and Anesin, 2012) or due to reworking (e.g., by bioturbation or freeze-thaw cycles), which Carcaillet (2001) reported for charcoal fragments from high altitude soils in the Alps. Also, radiocarbon ages derived from wood and charcoal might overestimate the true age, e.g., if the sampled material belongs to decay-resistant tree species, which may persist in the landscape long after the death of the tree (Schiffer, 1986). Traditional optical dating approaches (multi-grain and single-grain quartz and feldspar dating) are useful geochronological tools in some archaeological contexts (e.g., Junge et al., 2016). However, insufficient signal resetting causes significant challenges when these methods are applied to settings that are affected by slope processes (Fuchs and Lang, 2009), such as alpine dry-stone structures (e.g. Carrer and Angelucci, 2013).

Keeping these dating limitations in mind, rock surface luminescence has become a promising technique for dating archaeological contexts (e.g., Feathers et al., 2019; Galli et al., 2020; al Khasawneh et al., 2019; Sohbati et al., 2012a, 2015). The time of burial of rock surfaces can be dated by utilising the dose-dependent, light-sensitive luminescence signal, which accumulates in feldspar and quartz grains during burial. Exposure to daylight bleaches the luminescence signal in the rock surface grains within minutes to hours (Habermann et al., 2000; Vafiadou et al., 2007), and longer periods of exposure bleach the luminescence signal further into the rock (Gliganic et al., 2019; Ou et al., 2018; Sohbati et al., 2011, 2012b). Once the rock is buried, the dose in the bleached part of the rock (i.e., the bleaching front) increases due to radioactive decay. However, information regarding the depth of the bleaching front remains, even after burial. This is a significant advantage over conventional optical dating techniques in settings where bleaching conditions are less favourable since cobbles that were sufficiently exposed can be identified by the existence of luminescence signal-depth plateaus which are not saturated.

This study aims to investigate if rock surface luminescence dating is a viable dating method for chronologically constraining site formation of buried dry-stone structures in upland environments. To do so, we apply feldspar infrared stimulated luminescence (IRSL) dating to rock surfaces from cobbles collected from two archaeological units within a dry-stone structure from the Italian Alps. We compare our optical dating results to new and previously published radiocarbon ages. Furthermore, we offer new insight into the annealing of IRSL and post-infrared-IRSL (pIR-IRSL) signals in rocks.

2. Regional setting and site description

The study area is located in Val Poré, a tributary valley on the south-facing slope of the tectonic valley Val di Sole, Trentino, Italy (Fig. 1A). Local metamorphic rocks belong to the Ulten unit, which, together with the Tonale unit, forms the Tonale nappe in the Upper Austroalpine domain. The Tonale nappe is mainly made up of paragneiss, with intercalations of orthogneiss and mafic lithologies (Dal Piaz et al., 2007). The paragneiss (TUG in Fig. 1A) shows medium-high polycyclic metamorphism. The rock mainly features micas (both biotite and muscovite), quartz, sodium-rich feldspars, kyanites, and garnets. The paragneiss often displays compositional banding due to the alternation between micaceous layers and layers rich in quartz and feldspars. The orthogneiss (TUO in Fig. 1A) contains quartz, plagioclase, alkali feldspars, and micas (mostly biotite). The metamorphic overprinting of the Upper Austroalpine domain is polycyclic and covers a prolonged time interval, which includes a Palaeozoic phase (mostly Variscan) and an Eoalpine, Cretaceous phase. The orthogneiss intercalations, and the banding in the paragneiss, are parallel to regional schistosity and consistent with regional-scale foliation referring to the Variscan orogeny (Dal Piaz et al., 2007). The geomorphology of Val Poré is mainly dominated by glacial and periglacial processes (see Angelucci et al., 2014). The head of Val Poré is a glacial cirque filled with coarse talus and, on the eastern side, an active rock glacier that mainly consists of gneissic boulders. Downslope of the cirque, the rock glaciers appear mostly inactive. Gravitational and periglacial slope processes are also visible. Grasslands occur below the rock glaciers (∽2300 metres of elevation), exploited as grazing areas during the summer. Here podsols and cambisols (25–40 cm thick) cover the bedrock, moraine ridges, and relict rock glaciers. The landscape is affected by slope processes, most notably frost creep and gravitational slope deformations.

The chosen site for this study, MZ051S (Fig. 1B), is located at ∽2240 m above sea level in Val Poré. It is currently being investigated as part of the *Alpine Landscapes: Pastoralism and Environment of Val di Sole* (ALPES) project (e.g., Carrer and Angelucci, 2013; Angelucci et al., 2014; Carrer and Angelucci, 2018). This site is interpreted as a livestock enclosure, delimited by a collapsed dry-stone wall which is partly embedded in the topsoil (Fig. 1B). The dimensions of the enclosure are approximately 41 × 17 m, with the longer axis positioned with a north–south orientation. Fieldwork at the site has uncovered a ∽40 cm thick deposit which includes two archaeological units: US4a and US5a (Fig. 1C), both consisting of thin, poorly developed, buried A horizons. These horizons were developed from yellowish-brown silty loam (usually containing clasts of local gneiss), and later buried by colluvium derived from the erosion and re-deposition of former surface sediments and soil horizons, re-deposited from upslope of the site. Unit US4a yielded only scarce archaeological finds; several lithic and ceramic finds (knapped artefacts obtained from chert and potsherds) have been recovered from layer US5a (Angelucci et al., 2017). The units have previously been ^{14}C dated (Table 1) to Middle and Early Bronze Age, respectively (Angelucci et al., 2017). New radiocarbon ages (COL6511.1.1-COL6514.1.1), measured at the CologneAMS facility of University of Cologne (Dewald et al., 2013), verify US5a as Early Bronze Age, while also establishing a more complex chronology for US4a with the surprisingly young ^{14}C ages of 537–654 and 426–596 cal. AD. Younger and better preserved dry-stone structures have been surveyed in Val Poré and neighbouring tributary valleys (Carrer and Angelucci, 2013; Angelucci et al., 2014; Carrer and Angelucci, 2018). The largest of such structures (e.g., MZ005S; located at ∽2260 m above sea level in Val Poré) typically consist of a hut and four enclosures. These structures are associated with historic pastoral land use (Carrer and Angelucci, 2013) and have been constructed using local lithologies, mostly from paragneiss. The archaeological finds associated with MZ005S (Dell'Amore et al., 2017; Medici et al., 2014), and three ^{14}C samples (also from MZ005S) dated to the 7th, the 15th, and the 20th centuries AD (Angelucci and Carrer, 2015; Carrer and Angelucci, 2013), indicate that these still exposed structures were built between late Medieval to early Modern periods.

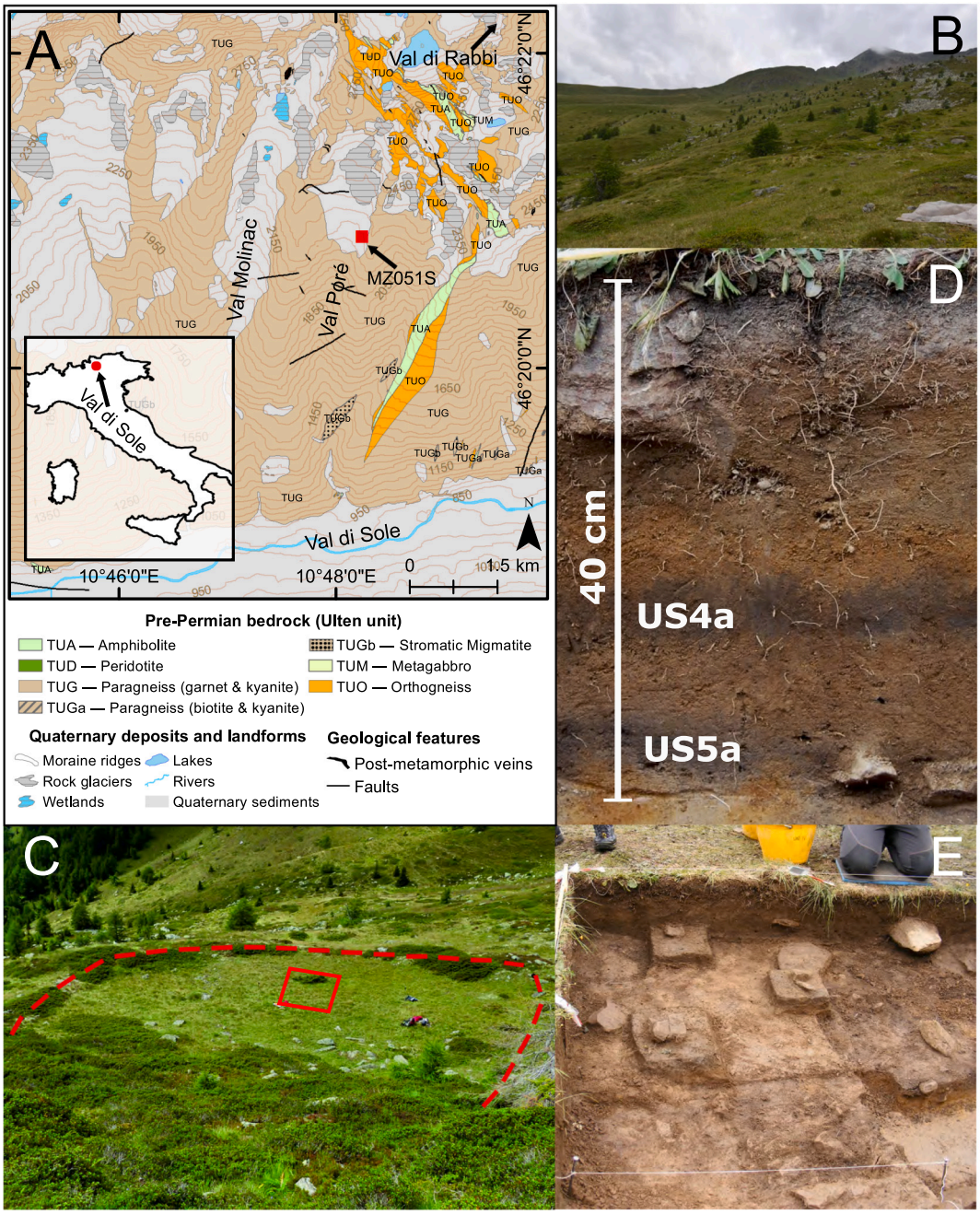

Fig. 1. (A) Geological mapping of the study area. Data visualisation: Geological Service of the Autonomous Province of Trento (Italy). (B) The landscape of Val Poré is dominated by grazed grasslands covering Quaternary sediments and gneissic bedrock. Gneissic boulders form a rock glacier, which southern snout is visible in the upper right corner. (C) Outline (dashed line) of MZ051S in Val Poré. The approximate location of the 2018 excavation is outlined (solid line) near the centre of the excavation. (D) The stratigraphic succession of MZ051S. Two archaeological units, US4a and US5a, have previously been described by Angelucci et al. (2017). C and D are modified after Angelucci et al. (2017). (E) Gneissic cobbles were excavated from the archaeological units inside MZ051S.

Table 1
Results from radiocarbon dating of charcoal fragments from MZ051S (Fig. A.1, Appendix). All radiocarbon ages (including previously published ages) were (re-)calibrated using OxCal 4.4.2 (Bronk Ramsey, 2009) with the IntCal 20 curve from Reimer et al. (2020) and are reported as before present (BP, present = AD 1950). The calibrated ages (AD/BC) are reported with 95.4% probability. Samples COL6511.1.1, COL6512.1.1, COL6513.1.1, and COL6514.1.1 were prepared according to the procedure described by Rethemeyer et al. (2019). Lab. ID COL = CologneAMS, University of Cologne, Germany; DSH = CIRCE, INNOVA SCARL, Italy.

Depth (m)	Lab. ID	Sample	Unit	$\delta^{13}C$ (‰)	Radiocarbon age (a BP)	cal. AD/BC	Previously published in:
0.20	COL6514.1.1	ID1216	US4a	−34	1476 ± 46	537-654 AD	
0.25	COL6511.1.1	RR68	US4a	−29	1550 ± 40	426-596 AD	
0.20	DSH6956	ID1145	US4a	−26	3225 ± 26	1532-1435 BC	Angelucci et al. (2017)
0.35	COL6512.1.1	RR100	US5a	−22	3296 ± 48	1731-1452 BC	
0.35	COL6513.1.1	ID1149	US5a	−24	3585 ± 46	2124-1773 BC	
0.25	DSH6955	ID1146	US5a	−20	3459 ± 23	1880-1691 BC	Angelucci et al. (2017)

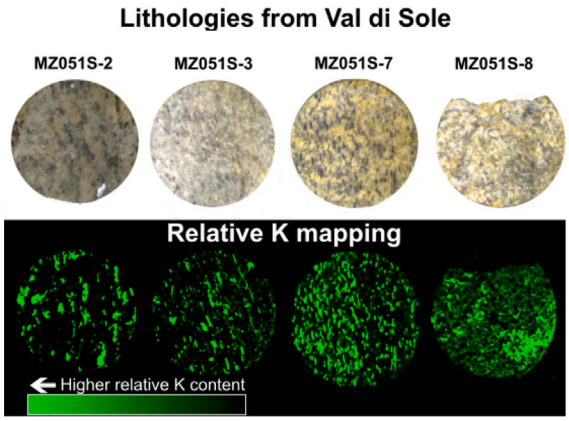

Fig. 2. Lithologies collected from the excavation of MZ051S in Val di Sole, Italy. The relative potassium concentrations within the slices were mapped with μXRF. Visual comparisons between the slices and the potassium maps show that areas of high relative potassium content mainly correlate with mica minerals (see also Fig. D.1, Appendix), not with potassium-rich feldspars. The slices are ∽10 mm in diameter.

Table 2
Overview of the cobbles dated in this study.

Lab code	Sample	Unit	Clast size (mm)	Lithology
C-L4626	MZ051S-2	US4a	100*x*80*x*70	Paragneiss (TUG)
C-L4627	MZ051S-3	US4a	100*x*60*x*30	Orthogneiss (TUO)
C-L4629	MZ051S-7	US5a	200*x*130*x*50	Paragneiss (TUG)
C-L4630	MZ051S-8	US5a	260*x*120*x*110	Paragneiss (TUG)

3. Methodology

3.1. Samples and preparation

Cobble-sized rocks, embedded in a scattered distribution within the excavated archaeological units (Fig. 1E), were sampled during a fieldwork campaign in July 2018. The cobbles were collected from an area of approximately 4 m^2. Due to the archaeological excavation, the top surfaces of some cobbles were exposed in the excavation for up to two days before sampling. After extraction, the cobbles were covered in aluminium foil and stored in opaque bags. Some cobbles were deemed inadequate for further preparation upon inspection in red-light condition due to their shape which would make extraction of intact cores difficult. We proceeded with two cobbles from each layer (Fig. B.1, Appendix): MZ051S-2 and MZ051S-3 from layer US4a, and MZ051S-7 and MZ051S-8 from layer US5a (Table 2). The cobbles originate from local outcrops of pre-Permian paragneiss (MZ051S-2, MZ051S-7, MZ051S-8) and orthogneiss (MZ051S-3). The cobbles demonstrate sub-angular morphology. MZ051S-2 is spherical, while MZ0051S-3, MZ051S-7, and MZ051S-8 have elongated shapes. All sample preparation and measurements were carried out in the Cologne Luminescence Laboratory at the University of Cologne, Germany. The cobbles were cored parallel to their shortest axis (MZ051S-2∽70 mm; MZ051S-3∽30 mm; MZ051S-7∽50 mm; MZ051S-8∽110 mm) with a water-cooled Proxxon TBH 28124 diamond-tipped bench drill, or with a water-cooled WEKA DK17 diamond core drill mounted on a stand. All cores were extracted more than 10 mm from the edge of the cobble to minimise the effect of signal resetting, which might have occurred when the sides of the cobbles had been exposed in the past. The cores were sliced into ∼0.7 mm thin round slices or irregular chips with a cooled Buehler Isomet 1000 precision saw. Charcoal pieces were prepared for AMS radiocarbon analysis using acid and alkali extraction and conversion of the organic carbon to elemental carbon by combustion and graphitization (Rethemeyer et al., 2019).

3.2. Measurements

All measurements were carried out with an automated Risø TL/OSL reader (model DA-20) (Bøtter-Jensen et al., 2010). For MZ051S-2 and MZ051S-3, whole slices were measured mounted directly in the sample carousel of the reader. This was not always possible for MZ051S-7 and MZ051S-8 since many slices broke during preparation, and thus, additional chips were measured in aluminium cups. A single aliquot regenerative (SAR) protocol (Murray and Wintle, 2000), modified for a low-temperature pIR-IRSL protocol with the post-infrared stimulation of 150 °C (e.g., Riedesel et al., 2018) (Table 3), was used to measure equivalent doses (D_e). Measurement time could be reduced by restricting the protocol to only measure the normalised, natural signal emission (L_n/t_n) for slices that were extracted from depths that were clearly in saturation. Dose–response curves (Fig. 3A–B) were fitted with exponential growth curves with the Luminescence Analyst v. 4.57 software (Duller, 2015). Beta irradiation was administered with a $^{90}Sr/^{90}Y$ beta source (∼0.088 Gy s^{-1}). Preheat (180 °C) was administered with a heating rate of 2 °C/s for 100 s. The slices/chips were stimulated with infrared light-emitting diodes (LED) (peak emission = 870 nm) at 50 °C (pIR-$IRSL_{150}$; step 4 and 9 in Table 3), followed by an additional infrared stimulation at 150 °C (pIR-$IRSL_{150}$; step 5 and 10 in Table 3). Emissions (insets in Fig. 3A–B) were filtered through an interference filter (410 nm) and detected with an Electron Tube PDM 9107Q-AP-TTL-03 blue/UV sensitive photomultiplier tube. Sample-dependent test doses varied between ∽2.5 and 8.7 Gy. We aimed at keeping the test dose ≤100% of expected D_e (determined by a dose test). A significant reduction in test dose–response (>40%) has been reported by Colarossi et al. (2018) for pIR-IRSL single grain data when applying a hot bleach at the end of the test dose cycle; results which are similar to those observed for our slices (Fig. 3C) when measured with IRSL protocol with a hot bleach at the end of the test dose cycle. To lessen this sensitivity change, Colarossi et al. (2018) proposed the use of a long, elevated IR stimulation (500 s at 225 °C) at the end of both the natural and test dose cycles to remove recuperation. Here, we use the low-temperature pIR-$IRSL_{150}$ protocol to prevent the sensitivity change between the natural and first test dose cycle (Fig. 3C). We measured additional slices from cobble MZ051S-2 with a pIR-$IRSL_{290}$ protocol (Table 3). We wanted to investigate the intensity of the optically less sensitive, high-temperature pIR-$IRSL_{290}$ signal (Kars et al., 2014) in the centre of this cobble when preliminary luminescence-depth measurement showed that it might have experienced heating.

Dose recovery tests were administered to three slices/chips per sample (bleached for 24 h in a Hönle solar simulator) to examine the ability of the SAR protocols to recover known beta doses of ∽2.6 to 21.9 Gy. Arithmetic mean dose recovery ratios (Fig. C.1, Appendix) are reported with and without subtraction of the dose residuals (Fig. C.2, Appendix). Dose recovery ratios (measured/given dose) range between 0.97–1.06 for the $IRSL_{50}$ signal and are thus near unity after subtraction of the residual dose. Without the subtraction, recovered doses for the $IRSL_{50}$ signal slightly overestimate but are still within 10% of the given dose. We did not use the pIR-$IRSL_{150}$ signal to date our samples due to the mostly poor dose recovery, both with or without residual subtraction (ratio range with subtraction: 0.75–1.31; without subtraction: 1.10–1.37). $IRSL_{50}$ residual doses from bleached slices/chips were low (< 0.5 Gy) except for MZ051S-7 (1.09 ± 0.35 Gy). The measured residuals range for the pIR-$IRSL_{150}$ signal is between 1.1 ± 0.1 to 3.8 ± 0.3 Gy. Dose recovery ratios for the pIR-$IRSL_{290}$ protocol were measured after 300 s of heating at 450 °C. The dose recovery ratio for this protocol is acceptable at 1.09 ± 0.19.

3.3. Effective dose rate throughout the cobbles

The radionuclide concentrations (Table 4) in the cobbles and the surrounding sediments were measured with high-resolution gamma spectrometry with a germanium detector for ∽42 h. One dose rate

Table 3
Overview of the low-temperature pIR-IRSL$_{150}$ and the pIR-IRSL$_{290}$ SAR protocols. The pIR-IRSL$_{150}$ protocol was applied to all rocks. The pIR-IRSL$_{290}$ protocol was only applied to MZ051S-2 to investigate the depth of resetting for the harder-to-bleach pIR-IRSL$_{290}$ signal. The IRSL$_{50}$ signal in pIR-IRSL$_{290}$ protocol was not used for any analysis since high preheat temperatures have shown to cause underestimation in the IRSL$_{50}$ signal (Li and Li, 2011a).

Step	Action		Signal	
	pIR-IRSL$_{150}$	pIR-IRSL$_{290}$	pIR-IRSL$_{150}$	pIR-IRSL$_{290}$
1	Irradiation	Irradiation		
2	Preheat (180 °C for 100 s)	Preheat (320 °C for 100 s)		
3	Pause (30 s)	Pause (30 s)		
4	IRSL (50 °C for 300 s)	IRSL (50 °C for 300 s)	L_x (IRSL$_{50}$)	
5	IRSL (150 °C for 300 s)	IRSL (290 °C for 300 s)	L_x (pIR-IRSL$_{150}$)	L_x (pIR-IRSL$_{290}$)
6	Irradiation	Irradiation		
7	Preheat (180 °C for 100 s)	Preheat (320 °C for 100 s)		
8	Pause (30 s)	Pause (30 s)		
9	IRSL (50 °C for 300 s)	IRSL (50 °C for 300 s)	T_x (IRSL$_{50}$)	
10	IRSL (150 °C for 300 s)	IRSL (290 °C for 300 s)	T_x (pIR-IRSL$_{150}$)	T_x (pIR-IRSL$_{290}$)

Table 4
Summary of radionuclide concentrations in the cobbles and the surrounding sediments, and the attenuated infinite matrix dose rates.

Sample	Sample type	Water content (%)	Radionuclide concentration				Dose rate (Gy ka-1)				
			^{238}U (ppm)	^{232}Th (ppm)	^{40}K (%)	InternalK (%)	Gamma	Beta	Alpha	Cosmic	Internal^{40}K
MZ051S-2	Cobble	0	1.96 ± 0.11	6.46 ± 0.42	1.11 ± 0.01	0.49 ± 0.08	0.81 ± 0.02	1.34 ± 0.02	0.04 ± 0.02	0.34 ± 0.03	0.012 ± 0.004
MZ051S-3	Cobble	0	2.88 ± 0.16	12.25 ± 0.74	0.89 ± 0.01	1.30 ± 0.15	1.14 ± 0.03	1.42 ± 0.03	0.06 ± 0.03	0.34 ± 0.03	0.042 ± 0.011
MZ051S-7	Cobble	0	2.34 ± 0.13	10.76 ± 0.63	1.00 ± 0.01	0.57 ± 0.09	1.04 ± 0.02	1.40 ± 0.03	0.05 ± 0.02	0.32 ± 0.03	0.014 ± 0.004
MZ051S-8	Cobble	0	0.69 ± 0.04	2.05 ± 0.14	0.52 ± 0.01	1.63 ± 0.15	0.57 ± 0.01	0.31 ± 0.01	0.01 ± 0.01	0.32 ± 0.03	0.039 ± 0.010
MZ051S-4a	Sediment	68 ± 6	4.68 ± 0.25	11.88 ± 0.62	2.49 ± 0.03		0.97 ± 0.05	1.61 ± 0.08	0.10 ± 0.04		
MZ051S-5a	Sediment	68 ± 6	5.51 ± 0.29	10.39 ± 0.62	2.17 ± 0.03		0.94 ± 0.05	1.50 ± 0.07	0.10 ± 0.04		

sample per cobble (∽200 grams each) was homogenised and allowed to rest for a minimum of three weeks to allow ^{222}Rn to reach equilibrium. For MZ051S-3, the majority of the cobble was crushed for dose rate measurements. For the other cobbles, cross-sections were cut to create representative subsamples. Radionuclide concentrations were converted to environmental dose rates with conversion factors reported by Cresswell et al. (2018). The average summer moisture content was calculated from moisture content upon sampling. The winter moisture content is assumed to be equal to the average saturated moisture content. We calculated the weighted average moisture content assuming three months of summer and nine months of winter, based on five soil samples. The moisture content in the cobbles is assumed to be negligible. We assume an average feldspar grain size of 400 μm for the cobbles. This is based on visual inspections of thin sections from previously collected rocks from the site. Depth-dependent, effective dose rates were calculated using the approach of Freiesleben et al. (2015), which uses the principle of superposition (Aitken, 1985) to scale the effective contribution of gamma and beta radiation to the cobbles based on infinite matrix dose rates derived from the sediments and the cobbles themselves. Attenuation factors of 1.89 and 0.01 for beta and gamma, respectively, were used to scale the attenuation of radiation (Aitken, 1985). The alpha radiation from the cobbles and surrounding sediments was not considered as the infinite matrix alpha dose rate was <4% of total dose rate in all samples, and thus, the effective alpha dose rate to 400 μm grains is considered to be negligible. The cosmic dose rate was assumed to be constant throughout the cobbles (Freiesleben et al., 2015) and was calculated using the *calc_CosmicDoseRate* function from the R-package *Luminescence* (Burow, 2019). Due to the shallow deposition depth, the function used data from Prescott and Hutton (1988, their Fig. 1) to estimate the soft and hard components of cosmic ray flux, and Prescott and Stephan (1982, their Eq. 1) to correct the cosmic component for altitude and latitude.

The internal potassium content of the feldspar grains within the cobbles was estimated with micro-X-ray fluorescence (μ-XRF), with a Bruker M4 Tornado μ-XRF spectrometer; an approach previously utilised by Rades et al. (2018). Relative element concentrations (potassium, calcium, aluminium, sodium, and silicon) were mapped on five slices per sample (Fig. D.1, Appendix). Visual comparison indicates that areas with relatively high concentrations of potassium align with the distribution of dark minerals (Fig. 2), which appear to have low concentrations of calcium and sodium. These darker grains are presumed to be micas, most likely biotites. We targeted feldspar grains by point measuring (spot size ∽20 μm) the non-mica grains which showed high concentrations of potassium, aluminium, calcium or sodium; elements which are abundant in feldspar. The acquired XRF spectra were analysed using the Bruker M4 Tornado software. A combined approach of fundamental parameter analysis and type calibration (Flude et al., 2017) with a feldspar standard was used to quantify element concentration in the slices. The average potassium concentrations of the feldspar grains in all rocks (Table 4) indicate significantly lower concentrations than the commonly assumed 12.5 ± 0.5% (Huntley and Baril, 1997) for alkali feldspars.

3.4. Fitting of luminescence-depth profiles

We fitted the luminescence-depth profiles in *R* v. 3.6.1 with the *nls* function from the *stats* package (R. Core Team, 2019). We applied the model (Table 5) developed by Freiesleben et al. (2015) to discern between exposure and burial events in our luminescence-depth profiles. The model uses the luminescence intensity (L), the saturated luminescence intensity (L_0), and the light attenuation coefficient (μ). Also, the model includes the exposure time (t_e) and the subsequent burial time (t_b). The rate of electron trapping: $F(x) = \frac{\dot{D}}{D_0}$ is included in the model, in which $\dot{D}$ is the effective dose rate at depth x, and D_0 is the characteristic dose. Average IRSL$_{50}$ luminescence-depth profiles were calculated from the individual cores. Individual μ values were determined for each surface by fitting; this, to allow for spatial variations of mineralogy within each of the cobbles. The sample-dependent average D_0 was constrained by exponential fitting of growth curves (highest irradiated dose >2800 Gy) and is assumed to be constant for all cores. The parameter $\overline{\sigma\varphi_0}$ describes the rate of emptying of traps based on the product of the photon flux and the photoionisation cross-section for $x = 0$. Since no exposure age calculations were attempted through fitting, $\overline{\sigma\varphi_0}$ was combined with t_e. No weights were applied during fitting. Fitting param are reported in Table 6 and fitting residuals are presented in Fig. C.3 (Appendix).

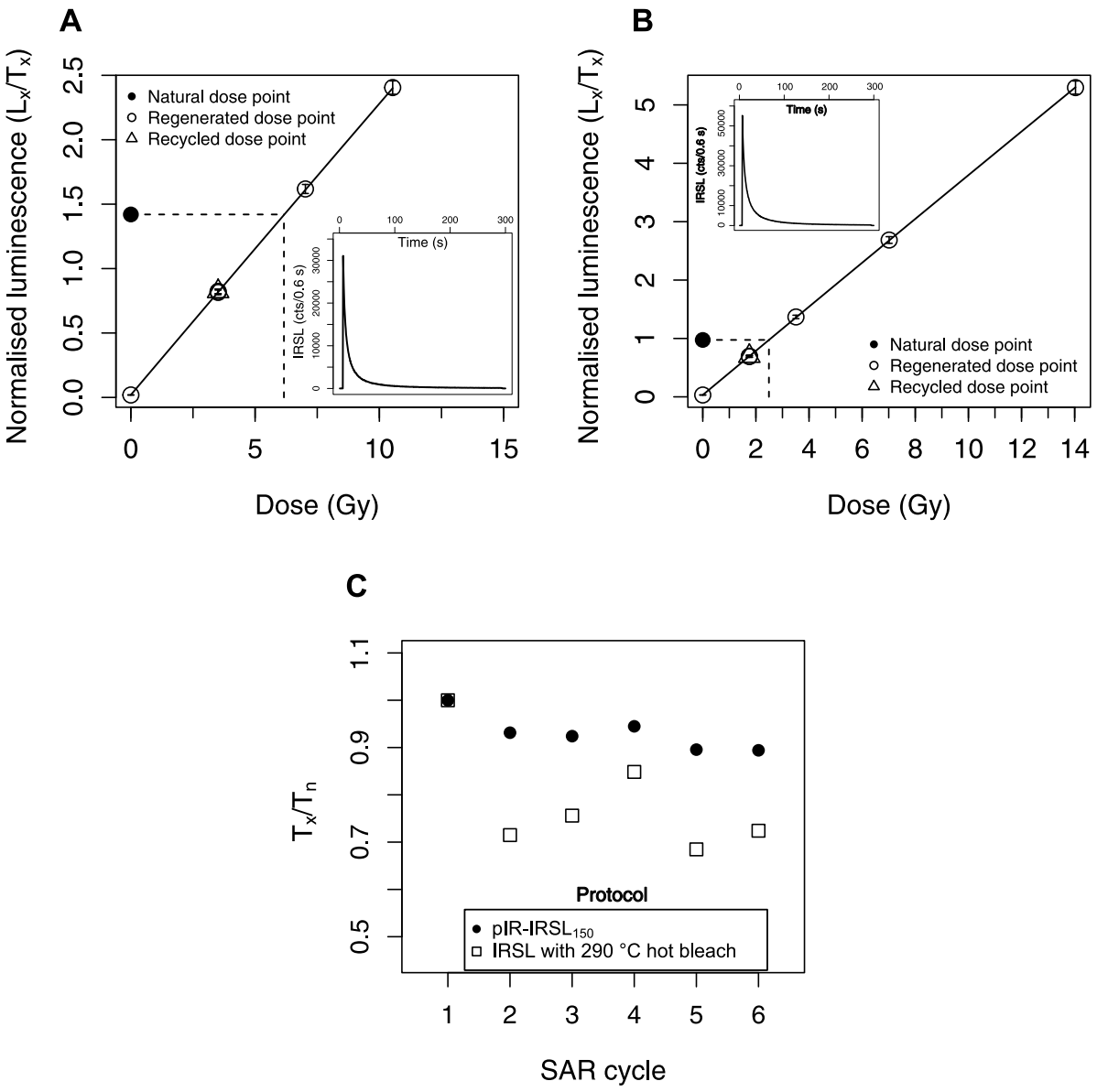

Fig. 3. Representative dose response curves for (A) MZ051S-2 (paragneiss) at ∽12 mm depth from the top surface, and (B) MZ051S-3 (orthogneiss) at ∽3 mm depth from the bottom surface. The insets show the natural $IRSL_{50}$ decay curve for the same slices. (C) Comparison of test dose response (T_x/T_n) from a paragneiss rock from Val di Sole, measured over several SAR cycles. The low-temperature pIR-IRSL protocol show significantly less change in test dose sensitivity, compared to an IRSL protocol with a hot bleach at the end of each cycle.

Table 5
Model developed by Freiesleben et al. (2015), used to fit burial and exposure events in the cobbles.

Event	Fitting model
Initial burial	$L_0(x) = 1$
First exposure E1	$L_1(x) = L_0(x)e^{-t_{e1}\overline{\sigma\varphi_0}e^{-\mu x}}$
First burial B1	$L_2(x) = (L_1(x) - 1)e^{-F(x)t_{b1}} + 1$
Second exposure E2	$L_3(x) = L_2(x)e^{-t_{e2}\overline{\sigma\varphi_0}e^{-\mu x}}$

3.5. Age calculations

The burial age can be calculated by either deriving the t_b parameter from the modelled exposure history of each rock surface (e.g., Freiesleben et al., 2015; al Khasawneh et al., 2019) or by estimating the burial dose by measuring D_e in slices from depths in which the signal was reset prior to burial (e.g., al Khasawneh et al., 2019; Rades et al., 2018; Sohbati et al., 2015). For our cobbles, we only consider the second approach reliable because we cannot detach the t_e and $\overline{\sigma\varphi_0}$ parameters, we have significant intra-core variations in our luminescence-depth profiles, and, as noted by al Khasawneh et al. (2019), t_b uses average D_0 values rather than individual D_0 values derived from dose–response curves from individual slices.

Instead, we calculated burial ages (ka before AD 2018) by dividing arithmetic mean D_e values derived from measuring slices/chips with depth-corrected dose rates. To identify which depths were suitable to use for D_e calculations (i.e. the slices had been sufficiently reset before burial), we applied the approach described by al Khasawneh et al. (2019). They proposed using the modelled luminescence-depth profiles to calculate a ratio between the pre-burial (E1; Table 5) and burial profiles (B1; Table 5). This ratio ($E1/B1$) represents the proportion of the burial dose, which is a pre-burial dose residual. Significant proportions of pre-burial dose indicate insufficient bleaching, which is undesirable for dating. We consider depths for which pre-burial dose

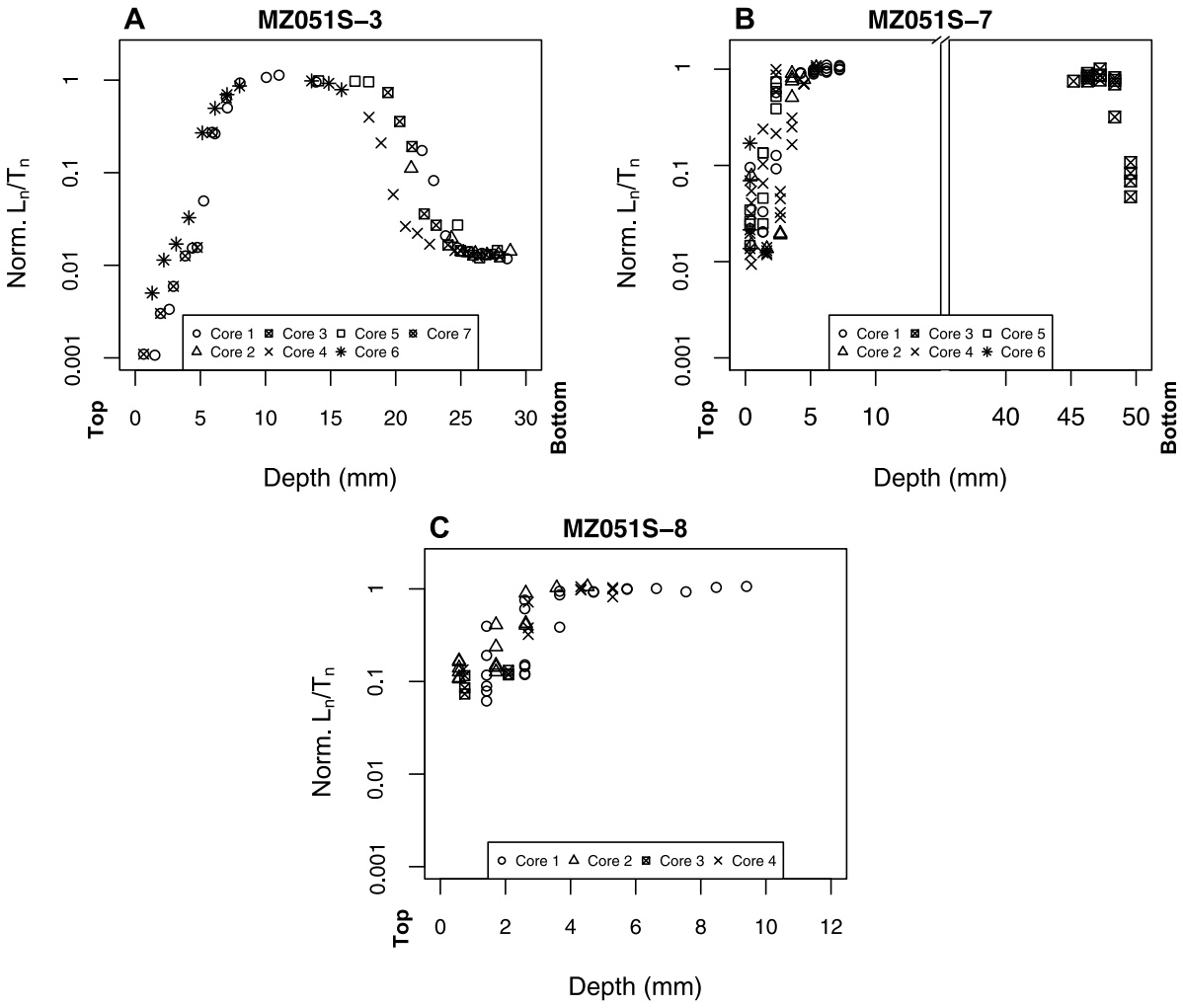

Fig. 4. $IRSL_{50}$ luminescence-depth profiles from individual cores from MZ051S-3 (A), MZ051S-7 (B), and MZ051S-8 (C). All data points represent one chip or slice. The $IRSL_{50}$ data are derived from IRSL stimulation at 50 °C in a pIR-$IRSL_{150}$ protocol. An overview of the measurement protocols is available in Table 3. The L_n/T_n data are normalised by the mean L_n/T_n data derived from the saturated dose plateau from the centre of the cobbles. The vertical axes of are plotted in logarithmic scale.

was modelled to constitute ≤1% ($E1/B1 \leq 0.01$) of the burial dose to have been fully reset. Therefore, burial ages were calculated from slices that were extracted from such depths. All luminescence ages are reported with 1-σ errors and measurement uncertainties.

3.6. Fading corrections

Anomalous fading (Wintle, 1977; Spooner, 1994) was measured using two different approaches. The first is the standard approach (Auclair et al., 2003) for sediment dating of feldspars, during which samples are irradiated and preheated in the laboratory, and the signal intensities are measured after different storage periods. For each cycle, the slices were irradiated with ∽8.9 Gy and storage periods ranged between prompt (i.e. no pause) to ∽17–33 h. For MZ051S-7, we added a measurement of signal loss after approximately 7 months of storage. Three slices per cobble were measured and cobble-specific, mean g-values were calculated from the results with the *analyse_FadingMeasurement* function (Kreutzer and Burow, 2020) in *R*. The mean g-values$_{2days}$ were calculated to 2.12 ± 0.67, 2.74 ± 0.57, 4.61±0.35 and 1.16±0.58 %/decade for MZ051S-2, MZ051S-3, MZ051S-7 and MZ051S-8, respectively (Fig. C.4, Appendix). Also, we measured g-values for four slices (storage up to 8 months) for the pIR-$IRSL_{290}$ protocol applied to MZ051S-2 (fading=1.63 ± 0.51%/decade). Ages were subsequently corrected using the procedure of Huntley and Lamothe (2001) with the *R* function *calc_FadingCorr* (Kreutzer, 2020).

The second approach uses the ratio between the intensity of the field saturation levels from the centre of the cobbles and the laboratory saturation level to correct for signal fading (Rades et al., 2018). The rationale behind this approach is that the field saturated signal should be in saturation; hence, the difference between the field saturated signal and the signal irradiated to saturation in the laboratory is assumed to arise from fading. The normalised natural signal (L_{nat}) and the saturated laboratory doses (L_{sat}) were measured for three slices per rock (doses >2800 Gy), and the average ratios were used to correct ages. The fading ratios L_{nat}/L_{sat} are 0.57±0.07 for MZ051S-3, 0.44±0.10 for MZ051S-7, and 0.52 ± 0.09 for MZ051S-8. This approach did not apply to MZ051S-2 since no slices were in saturation (see Section 4.1). Thus, for MZ051S-2, we were restricted to use only the conventional approach for fading correction since we lacked a field saturated signal to compare with.

4. Luminescence-depth profiles and burial ages

4.1. Luminescence-depth profiles

Here, we present $IRSL_{50}$ L_n/T_n data from individual cores as luminescence-depth profiles (Figs. 4 and 5). The depth of resetting of the $IRSL_{50}$ signal in the cobbles varies between different cobbles and surfaces. The luminescence-depth profiles from MZ051S-3 (Fig. 4A) demonstrate significantly larger L_n/T_n values at the centre, compared

Table 6
The parameters acquired from fitting luminescence-depth profiles.

Cobble	Surface	D_0 (Gy)	μ (mm^{-1})	$t_{e1}\overline{\sigma\varphi_0}$	$t_{e2}\overline{\sigma\varphi_0}$	t_b (ka)
MZ051S-3	Top	430 ± 30	0.91 ± 0.16	250 ± 261	4 ± 24	2 ± 5
MZ051S-3	Bottom	430 ± 30	0.65 ± 0.07	872 ± 699		2 ± 2
MZ051S-7	Top	615 ± 23	0.86 ± 0.13	10 ± 4		7 ± 9
MZ051S-7	Bottom	615 ± 23	1.18 ± 0.30	4 ± 2		
MZ051S-8	Top	467 ± 19	0.93 ± 0.20	9 ± 5		35 ± 17

to the top or bottom surface. The signal in the outer millimetres at the top surface has been bleached to <1% of the level measured in the centre of the cobble (field saturation). At ∽2 mm (core 6) or 3.5 mm (core 7) of depth, L_n/T_n is >1%. L_n/T_n increases deeper into the cobble until field saturation is reached at ∽7.5 mm of depth. At the bottom surface of MZ051S-3, all cores demonstrate a L_n/T_n plateau at between 1%–2% of field saturation until ∽5 mm (25–30 mm in Fig. 4A) of depth. Between ∽5–10 mm of depth (20–25 mm in Fig. 4A) L_n/T_n rises towards field saturation. Here, the luminescence-profiles differ between some of the cores; most notably the deeper bleaching front of core 4 compared to the other cores, and the shallower bleaching fronts of cores 1 and 5 compared to cores 2 and 3. At the top surface, cores 6 and 7 also demonstrate some scatter at ∽2–5 mm of depth. The luminescence-depth profiles ($IRSL_{50}$ data) from MZ051S-7 (Fig. 4B) demonstrate more shallow resetting compared to MZ051S-3. The luminescence-depth profiles for MZ051S-7 are mostly based on measurements of chips, not on whole slices, and these measurements demonstrate considerable intra-core variations between chips from the same depth within a single core. The bleaching front is shallow at the top surface since L_n/T_n is only below field saturation in the outer ∽4 mm of the rock. At the bottom surface, field saturation is reached already in the second slice. The surface slice at the bottom has a L_n/T_n of ∽8% of field saturation. In the top surface of MZ051S-8, L_n/T_n (Fig. 4C) increases from the surface, until ∽4 mm of depth. Like for MZ051S-7, the luminescence-depth profiles of MZ051S-8 are mostly based on chips, which demonstrate similar intra-core variations. At the top surface of MZ051S-2, L_n/T_n (Fig. 5) from $IRSL_{50}$ measurements increases without any obvious plateau from the surface until ∽5 mm of depth. Here, L_n/T_n plateaus, through the entire remaining depth of the cobble, until the bottom surface. The L_n/T_n values from this plateau are surprisingly low, considering the thickness (70 mm) of MZ051S-2. Despite using a test dose of only ∽4.3 Gy, the maximum L_n/T_n for the $IRSL_{50}$ signal we observe in any slice at any depth is < 3.0. The arithmetic mean L_n/T_n from this plateau is ∽1.3; assuming that field saturation L_n/T_n (measured with the same test dose) from the lithologically similar MZ051S-7 is applicable to MZ051S-2, then this is only ∽4% of the expected L_n/T_n if MZ051S-2 had a saturated signal plateau. Due to the lack of a saturated signal level, Fig. 5 is plotted without any normalisation. We measured L_n/T_n for the optically more stable pIR-$IRSL_{290}$ signal in four slices from the bottom surface, and seven slices from the centre of MZ051S-7. Overall, these L_n/T_n values are comparable (Fig. 5) to those determined from $IRSL_{50}$ measurements.

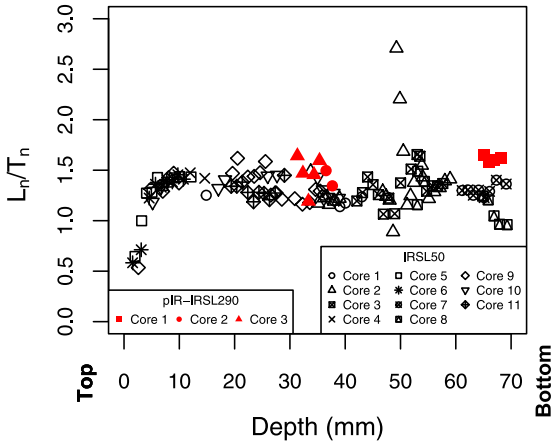

Fig. 5. $IRSL_{50}$ and pIR-$IRSL_{290}$ luminescence-depth profiles from individual cores from MZ051S-2. All data points represent one slice. The $IRSL_{50}$ data are derived from IRSL stimulation at 50 °C in a pIR-$IRSL_{150}$ protocol (Table 3). 97% of the slices from the plateau (5–70 mm of depth) are within 2σ of the mean. These L_n/T_n are not normalised (test dose ∽4.3 Gy) and are plotted on a linear vertical axis. The pIR-$IRSL_{290}$ data are derived from additional slices, which were stimulated at 290 °C after an initial stimulation at 50 °C (Table 3).

4.2. Fitting

Here, we present fitting of averaged luminescence-depth profiles (for the $IRSL_{50}$ signal) (Fig. 7) and their corresponding model parameters (Table 6). No fitting is attempted for MZ051S-2 since $L_0(x)$ is not known for this cobble. The top surface for MZ051S-3 is best fitted with two exposure events ($E1_{top}$, and $E2_{top}$), separated by a burial event ($B1_{top}$). The bleaching front of $E1_{top}$ appears to have reached ∽4 mm of depth before burial during $B1_{top}$. The second exposure event $E2_{top}$ appear to be shorter than $E1_{top}$, and only the outer ∽2.5 mm appear to have been affected. The fitting of the bottom surface is challenging due to the large inter-core variations in L_n/T_n at depths >5 mm. Visual inspections of the luminescence-depth profiles from the individual cores clearly show a single exposure event, followed by a single burial event. Keeping this in mind, we fit the averaged luminescence-depth profile for the bottom surface for a single exposure event ($E1_{bottom}$) and for a single burial event ($B1_{bottom}$) despite the poor fit at depths >6 mm from either surface (Fig. C.3, Appendix). The bleaching front of $E1_{bottom}$ reset the signal <1% of $L_0(x)$ to ∽7 mm of depth from the bottom surface. While there is no ambiguity regarding the thoroughness of resetting on the bottom surface of MZ051S-3, the ratio $E1_{bottom}/B1_{bottom}$ (Fig. 7A2) show that $B1_{bottom}$ contains no significant pre-burial dose at depths between ∽23–30 mm. The severe resetting (<1%) of the $IRSL_{50}$ signal in the top surface of MZ051S-3 suggests that no burial age can be calculated from D_e values from slices located at <3 mm of depth. However, since the fitting indicates the presence of a weak burial plateau between 3 mm and 4 mm we will proceed to use D_e values from slices extracted from this depth to calculate a burial age for $B1_{top}$. The top surface of MZ051S-7 has been fitted for an exposure event ($E1_{top}$), followed by a burial event ($B1_{top}$). While the observed signal plateau at this surface is very short, the $IRSL_{50}$ signal appears to have been sufficiently reset during $E1_{top}$ to create a bleaching front which reached >0.5 mm. The ratio $E1_{top}/B1_{top}$ (Fig. 7B.2) shows that <1% of the observed dose was present before burial. Thus, despite the weak signal plateau of only 2 mm, we proceed to calculate a burial age from the top surface of MZ051S-7. The modelled pre-burial luminescence-depth profile from the bottom surface predicts that signal resetting was insufficient the last time this surface was exposed to create a bleaching front even at the very surface of the cobble. This suggests that no information regarding the last burial is available from the bottom surface of MZ051S-7. For MZ051S-8 (Fig. 7C.1), we fit the top surface for an exposure event ($E1_{top}$) and a subsequent burial event ($B1_{top}$). Sufficient bleaching appears to have occurred during $E1_{top}$ to reset the $IRSL_{50}$ signal beneath the surface. The subsequent $B1_{top}$ event should therefore date the last burial of this rock surface. The $E1_{top}/B1_{top}$ ratio from the fitting (Fig. 7C.2) indicates that ∽1% of the observed dose is

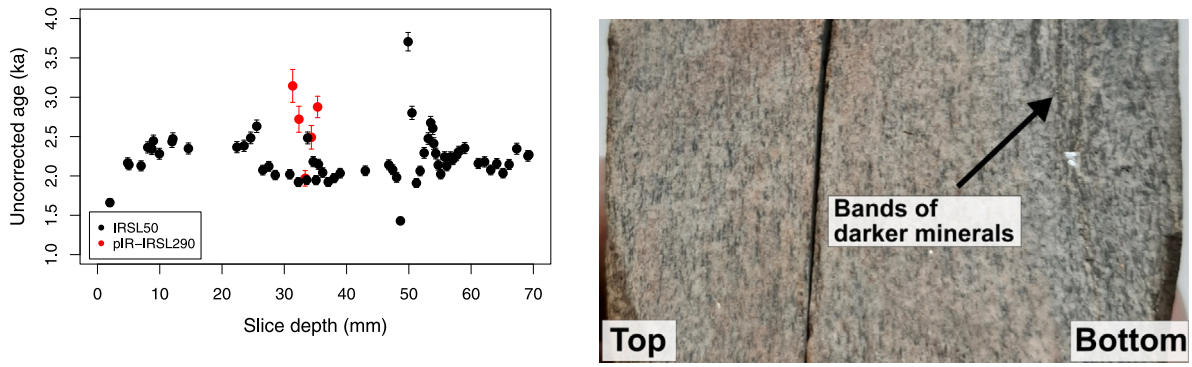

Fig. 6. (Left) $IRSL_{50}$ and pIR-$IRSL_{290}$ ages, calculated throughout cobble MZ051S-2 (n=1). The ages have not been corrected for fading. The error bars represent uncertainties from D_e and dose rate measurements. (Right) cross-cut of MZ051S-2 along the cored axis. Approximately 0.5 mm of the rock is missing due to a previous cut across the cored axis. The scatter in the age data around 50 mm of depth appear to coincide with a band of dark minerals.

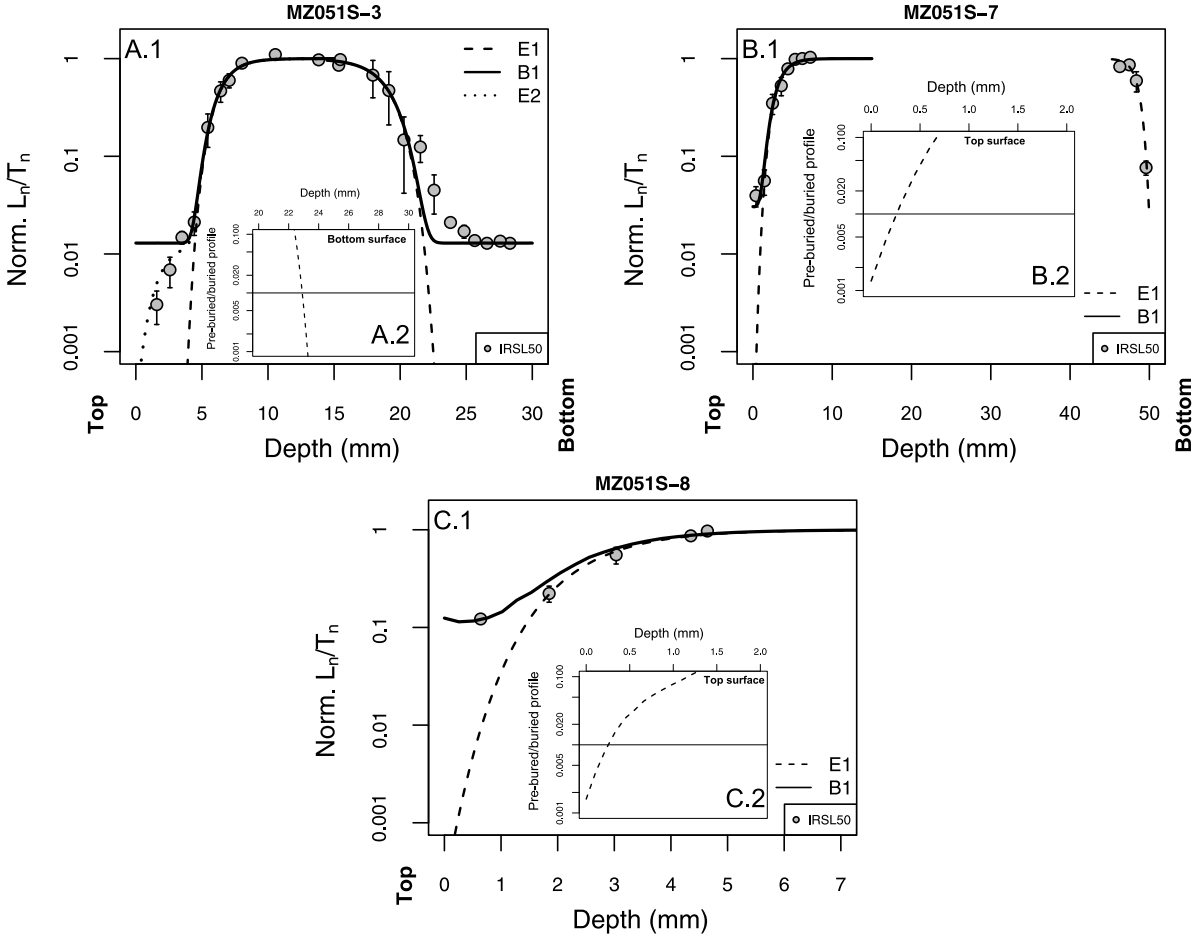

Fig. 7. Averaged (n≥2) $IRSL_{50}$ luminescence-depth profiles and their corresponding fits with the Freiesleben et al. (2015) model from MZ051S-3 (A), MZ051S-7 (B), and MZ051S-8 (C). The normalised sensitivity-corrected luminescence signals (L_n/T_n) are plotted in logarithmic scale. The dashed lines in the insets show the ratios (E/B) between modelled exposure events (E) and modelled burial event (B) with depth.

pre-burial in the surface slice. Therefore, a burial age from the surface slices should not be affected by inherited dose from a previous event.

4.3. Burial ages

Burial ages for the four cobbles are presented in Table 7. Considering the similarity in L_n/T_n in the non-saturated plateau (∽5–70 mm) in MZ051S-2, we interpret this to represent an isochronous resetting event which can be dated using SAR protocols (Table 3). Since this plateau is manifested over significant depth-distances in the cobble (∽65 mm), we would expect the effective dose rate to vary between some of the slices. Therefore, we calculate the age for each slice individually before averaging the age over the entire plateau, instead of using the approach described in Section 3.5. For the $IRSL_{50}$ signal, we calculate an arithmetic mean age from 62 slices collected varying depths of the plateau (Fig. 6A). The same approach was used to calculate pIR-$IRSL_{290}$ ages from five additional slices (Fig. 6A). The $IRSL_{50}$ uncorrected ages throughout this signal plateau range between 1.4 and 4.6 ka, with an arithmetic mean age estimate of 2.23 ± 0.61 ka. The uncorrected pIR-$IRSL_{290}$ ages range between 2.00 and 3.19 ka, with the arithmetic mean

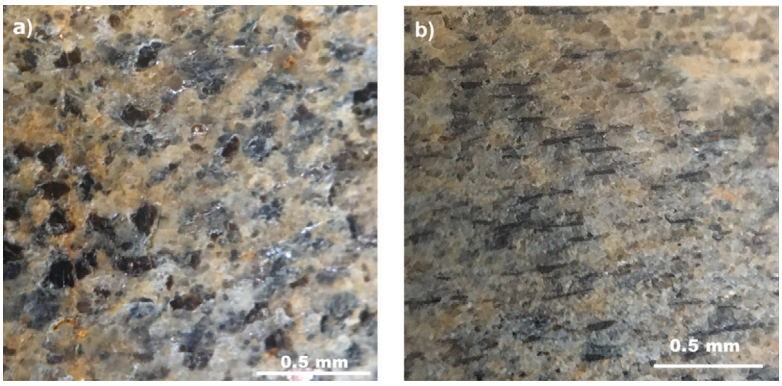

Fig. 8. The mica grains in the paragneisses in Val di Sole show distinct foliation. The readers view direction is perpendicular onto (a), and parallel to (b) the metamorphic foliation.

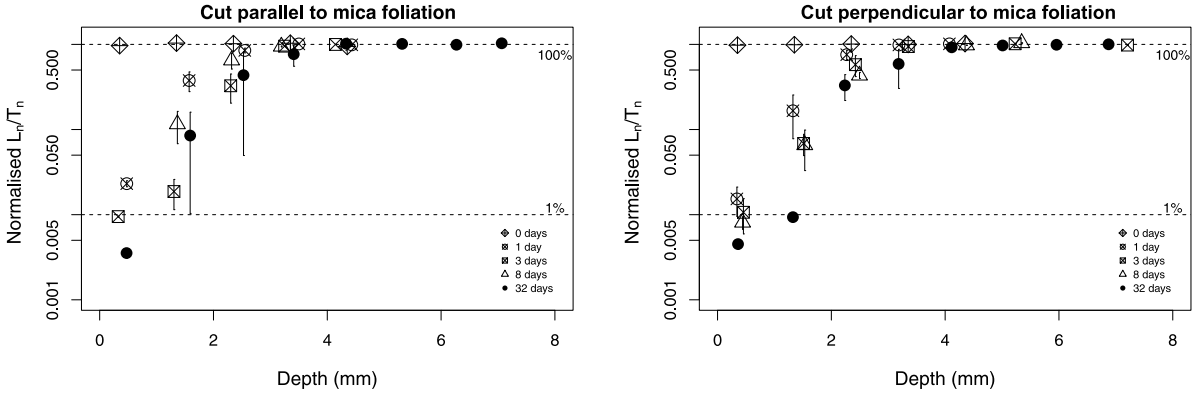

Fig. 9. The luminescence-depth profiles (n=2, except for 0 days for which n=1) from MZ051S-7, measured in fresh rock surfaces which had been exposed on a rooftop in Cologne, Germany for: 0, 1, 3, 8, and 32 days. The cores were extracted from surfaces which were cut parallel (left) and perpendicular (right) to the mica foliation. The error bars represent 1σ. The dashed lines represent 1% and 100% of the saturated $IRSL_{50}$ intensity L_0, respectively.

age estimate of 2.68 ± 0.55 ka. Fading correction with g-values (Auclair et al., 2003; Huntley and Lamothe, 2001), yield corrected ages of 2.64 ± 0.75 ka (1370 BC–130 AD) and 3.03 ± 0.67 ka (1680–340 BC) for the $IRSL_{50}$ and $IRSL_{290}$ protocols, respectively. The luminescence-depth profile from the outer ∽4 mm of the top surface of MZ051S-2 (Fig. 4A) indicates that some resetting of the signal has occurred after the previously described resetting event. We measured the D_e of one slice from ∽2 mm depth to date this event. The resulting $IRSL_{50}$ age estimate for this slice yields an uncorrected burial age of 0.85 ± 0.10 ka and a corrected burial age of 1.00 ± 0.13 ka (890–1150 AD). We calculate the burial age from two slices (3–4 mm of depth) from the top surface of MZ051S-3 which yields an uncorrected arithmetic mean age of 1.08 ± 0.08 ka. For the bottom surface, we calculate the arithmetic mean $IRSL_{50}$ age of five slices from ∽2 mm of depth. The uncorrected mean age is 0.86 ± 0.05 ka. When corrected with the measured g-value, the top surface dates to 1.34 ± 0.13 ka (550–810 AD), and the bottom surface dates to slightly younger: 1.05 ± 0.09 ka (880–1060 AD). Fading corrections with the L_{nat}/L_{sat} fading ratio yields older ages of 1.90 ± 0.24 ka (120 BC–360 AD) for the top surface and 1.51 ± 0.18 ka (330–690 AD) for the bottom surface. For MZ051S-7, we calculate a burial $IRSL_{50}$ age by measuring D_e measurements on three intact surface slices. Age calculations yield an uncorrected burial age of 2.19 ± 0.24 ka. Again, the fading-corrected ages vary depending on which fading correction method we apply. Fading correction with g-value yields an age of 3.11 ± 0.37 ka (1460–720 BC), compared to the considerably older age of 4.99 ± 0.51 ka (3480–2460 BC) with the L_{nat}/L_{sat} ratio correction method. D_e measurements from 12 surface chips from the top surface of MZ051S-8 yield an uncorrected arithmetic mean age of 16.9 ± 1.9 ka; much older than the expected age. Fading correction with g-value increases the age estimate to 18.7 ± 2.3 ka. Correcting the age estimate with L_{nat}/L_{sat} ratio increases the age further to 38.3 ± 9.7 ka.

5. Bleaching experiment

The results presented in Section 4 show that while at least some resetting has occurred in all cobbles, the bleaching fronts, especially for MZ051S-7 and MZ051S-8, are shallow. The $E1_{top}/B1_{top}$ ratios for both these cobbles indicate that the pre-burial dose constitutes significant proportions of the buried dose already at 0.5 mm of depth (see insets in Fig. 7B–C). We would expect deeper bleaching in rock surfaces that should have experienced significant exposure. One possible explanation for these shallow bleaching fronts is erosion. While erosion of rock surfaces has been shown to affect the depth of the bleaching front (Sohbati et al., 2018; Lehmann et al., 2020), in the given case, we cannot quantify erosion rates since we lack independent dates for how long these surfaces were exposed before burial. An alternative explanation for shallow depth-profiles is strong attenuation of light due to lithological parameters (e.g., Ou et al., 2018). We investigate the effect of light penetration on the resetting of the $IRSL_{50}$ signal in MZ051S-7 and which potential effect the mineral orientation may have on the rate of resetting. The paragneisses from Val Poré have a distinct orientation of mineral foliation (Fig. 8), and dark mica minerals are common. The occurrence of dark minerals has shown to block the bleaching of the luminescence signal in minerals beneath (Meyer et al., 2018). Visual inspection of a thin section from a paragneiss from the relevant geological unit clearly shows mica grains surrounding the more translucent quartz and feldspar grains (Fig. B.2, Appendix). If the attenuation of light penetration into the rock is weaker at surfaces with planes perpendicular to the foliation (with a lower surface area

Table 7
Summary of uncorrected and fading corrected $IRSL_{50}$ ages, number of slices used for age estimation (n), dose rate for surface slices, normalised g-values, and L_{nat}/L_{sat} ratios.

Sample	Protocol	Part of rock	Dose rate surface slice (Gy ka^{-1})[a]	g-value $_{2days}$ (%/decade)	Fading ratio[b]	Mean D_e (Gy)[c]	n	Uncorr. age (ka)	Corr. age[d] (ka)	Corr. age[e] (ka)	Corr. age[d] (AD/BC)	Corr. age[e] (AD/BC)
MZ051S-2	$IRSL_{50}$	Top	2.74 ± 0.06	2.05 ± 0.55		2.28 ± 0.05	1	0.85 ± 0.10	1.00 ± 0.13		890–1150 AD	
MZ051S-2	$IRSL_{50}$	Centre-bottom	2.74 ± 0.06	2.05 ± 0.55		5.93 ± 1.19	62	2.23 ± 0.61	2.64 ± 0.75		1370 BC–130 AD	
MZ051S-2	pIR-$IRSL_{290}$	Centre	2.74 ± 0.06	1.63 ± 0.51		7.11 ± 1.38	5	2.68 ± 0.55	3.03 ± 0.67		1680–340 BC	
MZ051S-3	$IRSL_{50}$	Top	2.85 ± 0.06	2.74 ± 0.57	0.57 ± 0.07	3.03 ± 0.21	2	1.08 ± 0.08	1.34 ± 0.13	1.90 ± 0.24	550–810 AD	120 BC–360 AD
MZ051S-3	$IRSL_{50}$	Bottom	2.85 ± 0.06	2.74 ± 0.57	0.57 ± 0.07	2.41 ± 0.13	5	0.86 ± 0.05	1.05 ± 0.09	1.51 ± 0.18	880–1060 AD	330–690 AD
MZ051S-7	$IRSL_{50}$	Top	2.73 ± 0.06	4.61 ± 0.34	0.44 ± 0.10	5.98 ± 0.54	3	2.19 ± 0.24	3.11 ± 0.37	4.99 ± 0.51	1460–720 BC	3480–2460 BC
MZ051S-8	$IRSL_{50}$	Top	1.91 ± 0.06	1.16 ± 0.58	0.52 ± 0.09	27.67 ± 2.26	12	16.87 ± 1.90	18.66 ± 2.34	38.33 ± 9.72		

[a]Integrated over 0 to 0.7 mm of depth.
[b]Fading ratio (L_{nat}/L_{sat}).
[c]Errors include standard error (1σ) and measurement uncertainties.
[d]Fading correction with g-value (Huntley and Lamothe, 2001).
[e]Fading correction calculated by dividing uncorrected age by fading ratio.

covered by mica minerals), then these surfaces should be targeted during sampling. Unbleached surfaces were exposed on a rooftop of the University of Cologne, Germany, during the summer of 2019. We sampled the exposed surfaces after 0, 1, 3, 8, and 32 days and subsequently measured the luminescence-depth intensity of two cores for each surface and each period of exposure (Fig. 9). The signal is, as predicted, in saturation throughout the cores that have not been exposed (0 days of exposure). The surface slices in all other cores have been bleached <5% of saturated IRSL. L_n/T_n is less than 1% in the surface slice after three days at the rooftop in optimal bleaching conditions (e.g., a fresh surface, many hours of daylight in sunny weather, and no coverage of sediments or lichen). After 32 days of exposure has L_n/T_n been reset to <0.5% of saturation at the surface. The $IRSL_{50}$ signal reaches 95% of field saturation between 3.2 mm (1 day of exposure) and 4.1 mm (32 days of exposure) of depth in the cores cut parallel to the foliation. This is similar to cores cut perpendicular to the foliation for which the signal reaches field saturation between 3.5 mm (1 day of exposure) and 4.3 mm (32 days of exposure). Our experiment shows that residual $IRSL_{50}$ signals in the surface slice in paragneiss rock surfaces from Val di Sole can be expected to be beneath 1% of field saturation after three days of exposure. Both surfaces did bleach during exposure; however, resetting appears to occur slightly quicker in the surface cut perpendicular to foliation. It is not possible, based on our experiment, to assert if the shallow bleaching profiles observed in the natural paragneisses are due to erosion or insufficient light penetration, but simulated profiles (Fig. 10) indicate that exposure periods longer than a decade would bleach the signal to 5 mm or more.

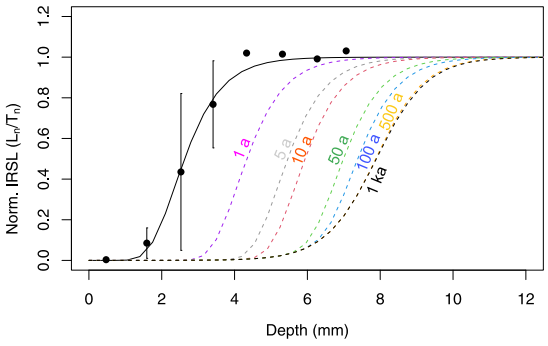

Fig. 10. Modelled luminescence-depth profiles, simulated (dashed lines) for different exposure durations for MZ051S-7. The parameters μ (1.42 ± 0.18 mm^{-1}) and $\overline{\sigma\varphi_0}$ (333 ± 158 a^{-1}) were derived by fitting (solid line) the signal profile (non-weighted) from a surface exposed on the rooftop in Cologne (Fig. 9, 32 days of exposure of surface cut parallel to the mica foliation) with the model: $L(x) = \frac{\overline{\sigma\varphi_0}e^{-\mu x}e^{-t_e(\overline{\sigma\varphi_0}e^{-\mu x}+F(x))}+F(x)}{\overline{\sigma\varphi_0}e^{-\mu x}+F(x)}$ developed by Sohbati et al. (2012c). $F(x)$ was constrained as described in Section 3.4.

6. Discussion

6.1. Signal resetting in the cobbles

Rock surface luminescence dating of buried cobbles is only possible if the luminescence signals can be reset during exposure to light or heat. A previous study by Ou et al. (2018) demonstrated little or no depletion in $IRSL_{50}$ and pIR-IRSL signals in some lithologies during lengthy exposure. Three of the cobbles (MZ051S-3, MZ051S-7, MZ051S-8) presented in this paper demonstrate significantly lower (approximately one order of magnitude or more) L_n/T_n towards the edges of the cobbles, compared to their respective centres. This, together with the data presented in Fig. 9, shows that some resetting in the outer millimetres of our cobbles will occur if the surfaces are exposed for at least four weeks. The resetting appears to occur even quicker in MZ051S-3, based on the observed resetting ($E2_{top}$) of the top surface, which we interpret to have occurred while the surface was exposed in the excavation; a reasonable assumption since the cobble was completely covered before being excavated. Overall, MZ051S-3 displays considerable inter-core variations for the depth of resetting. These variations become apparent when we fit the averaged luminescence-depth profiles with the Freiesleben et al. (2015) model. Fitting of an average luminescence-depth profile is challenging when fitted with average μ and $t_e\overline{\sigma\varphi_0}$ values since these parameters do not consider small-scale mineralogical variation or uneven spatial erosion of the rock surface. Spatially uneven light attenuation due to the presence of darker minerals is a problem in banded metamorphic rocks (Meyer et al., 2018); this is likely affecting our cobbles too.

The outer 0.5 mm from the top surface of MZ051S-7 appear to have been bleached before burial, which is demonstrated by the $E1/B1$ ratio (Fig. 7B.2) ∽0.01. This is a shallow luminescence-depth profile considering that simulated luminescence-depth profiles (Fig. 10) indicate that exposure periods longer than one year would bleach the signal 2 mm into the rock or more. While we cannot be certain regarding the length of exposure of the top surface from MZ051S-7, the formation of an A horizon (US5a) suggests extended exposure of this unit before being buried by colluvium. The luminescence-depth profile of MZ051S-8 displays a similar pattern with a short bleaching front. Erosion would likely have shortened the bleaching front of the luminescence-depth profile of these two cobbles if they were exposed for extended periods (e.g., one year or longer).

The measured chips from MZ051S-7 show significant intra-core variation for the luminescence intensity, for which the underlying reason is currently not understood. To circumvent the problem of intra-core variations, we exclusively derive the burial age of the top surface of MZ051S-7 from three intact surface slices. The bottom surface of

MZ051S-7 was insufficiently bleached or eroded before burial and thus, does not provide significant information regarding the cobble's history.

The lack of a saturated $IRSL_{50}$ (or pIR-IRSL) signal plateau throughout MZ051S-2 is an interesting and unexpected observation. The extensive period between the cooling of the minerals after the rock formation and sampling is well beyond the saturation limit for any luminescence signal, and thus, the electron traps in the mineral crystals in the centre of the rock must have been emptied during a later event. There is some scatter observed in the luminescence-depth profile, especially around 50 mm of depth (Fig. 4A). This area of scatter appears to coincide with a mineralogical change towards a more prominent foliation of dark minerals (Fig. 6). Possibly, these darker areas represent an area with a higher dose rate. It is unlikely that these outliers represent a different event than the other slices from the centre of MZ051S-2. None of them appears to be close to saturation, and they do not form a visible plateau. Hence, despite this scatter, we interpret the luminescence-depth profile presented in Fig. 4A as an isochronous dose plateau (excluding the top ∽5 mm). Therefore, a resetting event must, at some point in the past, have depleted the luminescence signals throughout the entire cobble. Complete optical resetting of the luminescence signals throughout MZ051S-2 during light exposure is unlikely. When we model the rate of resetting of the IRSL signal in MZ051S-7 (i.e. a rock of similar lithology) with the model by Sohbati et al. (2012c), the simulated profiles indicate that optical resetting to the centre of the cobble is not possible (Fig. 10), even if the rock surface experienced no erosion during exposure. Furthermore, the resetting of the $pIR\text{-}IRSL_{290}$ signal within the centre of the cobble by optical resetting is even more unlikely, considering the hard-to-bleach character of the $pIR\text{-}IRSL_{290}$ signal demonstrated by laboratory bleaching experiments (Kars et al., 2014) and published $pIR\text{-}IRSL_{290}$-depth profiles from cobbles (Freiesleben et al., 2015). In contrast, heat could effectively reset both the $IRSL_{50}$ and the $pIR\text{-}IRSL_{290}$ signals. Previous investigations of thermal stability of the $IRSL_{50}$ signal with pulse annealing (Murray et al., 2009; Li and Li, 2011b; Thomsen et al., 2011) have demonstrated that the $IRSL_{50}$ signal is thermally reset by short exposures (60 s or less) to temperatures >450 °C. Elevated temperature pIR-IRSL signals are more thermally stable (Li and Li, 2011b; Thomsen et al., 2011), but do nevertheless deplete at temperatures >550 °C (Thomsen et al., 2011). A thermal reconstruction of a prehistoric hearth by Brodard et al. (2012) indicated that such a feature could reach temperatures >600 °C. No hearth has so far been discovered during excavations in Val Poré, but fire has likely been present at the site. This is demonstrated by the charcoal fragments and fire modified artefacts, collected from the archaeological units (Angelucci et al., 2017). While further investigations of the thermoluminescence characteristics of MZ051S-2 would be necessary to determine the duration and temperature of the heating events, the complete resetting throughout the cobbles would require extensive heat during longer periods, e.g., in a hearth, or, perhaps, during a forest fire. However, at our site, no other cobbles show any signs of resetting in the middle of the cobbles. The isolated observation of extreme resetting in MZ051S-2 indicates selective heating, unlikely to occur during a forest fire. Therefore, we find that the resetting of the centre-bottom part of MZ051S-2 is analogous to a heating event which most likely was induced by human activities at the site during the Late Bronze Age or during the Iron Age. We observe no signs of any subsequent resetting event on the bottom surface of the cobble, which indicates that the bottom surface did not see significant exposure following the heating. This interpretation implies lengthy exposure of the top surface of MZ051S-2 as part of the topsoil; such exposure should bleach to over 5 mm of depth as is indicated by the simulation exposure periods presented in Fig. 10. The bleached (and subsequently buried) profile at the top surface is, while deeper than the bleached profile of e.g., MZ051S-7, slightly shallower than expected for such a long exposure. Erosion is also here a likely but untested explanation.

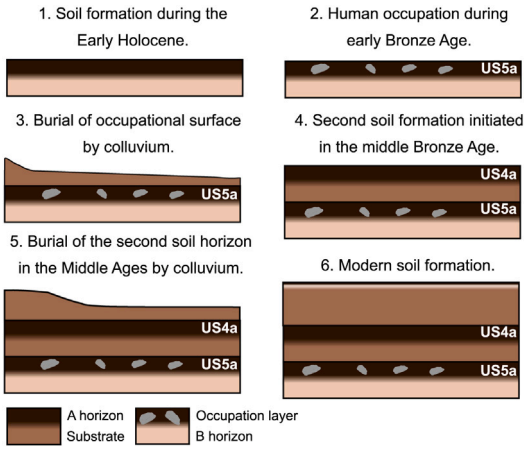

Fig. 11. Schematic illustration of the site formation of MZ051S, based on stratigraphy, radiocarbon dating (Table 1) and rock surface $IRSL_{50}$ dating (Table 7).

6.2. Fading estimates

For our cobbles, the application of g-value corrections (Huntley and Lamothe, 2001) yields significantly different ages compared to the L_{nat}/L_{sat} ratio (Rades et al., 2018). All conventional $IRSL_{50}$ g-values (∽2–5%/decade) do not differ significantly to the average g-values reported by Thomsen et al. (2008) for potassium-rich (3.0 ± 0.1%/decade) and sodium-rich (3.1 ± 0.2%/decade) feldspar extracts from sediments of various geographical and sedimentological origins. The $pIR\text{-}IRSL_{290}$ signal from MZ051S-2 fades at a similar rate as is reported by Sohbati et al. (2013) for sodium-rich feldspars (∽0.2–2.2%/decade) measured with a $pIR\text{-}IRSL_{290}$ protocol. The apparent thermal resetting of MZ051S-2 grants us the possibility to compare our g-value corrected $IRSL_{50}$ age with the uncorrected and corrected $pIR\text{-}IRSL_{290}$ ages. The $IRSL_{50}$ and $pIR\text{-}IRSL_{290}$ ages agree within uncertainties. This is encouraging, especially since our laboratory experiments with the $pIR\text{-}IRSL_{290}$ protocol show acceptable dose recovery. Previously, $pIR\text{-}IRSL_{290}$ dating of heated stones has been successfully compared to OSL dating of quartz (al Khasawneh et al., 2015), and $pIR\text{-}IRSL_{290}$ dating has repeatedly been demonstrated to be accurate when compared with other luminescence dating techniques or dating methods (e.g., Buylaert et al., 2012; Murray et al., 2014; Klasen et al., 2018; Zander et al., 2019). Based on the agreement between the $IRSL_{50}$ and $pIR\text{-}IRSL_{290}$ in MZ051S-2 and previous successful applications of $pIR\text{-}IRSL_{290}$ dating, we propose that the g-value corrected ages in Table 7 are the preferred ages to use for chronostratigraphic interpretations. However, the extrapolation of this rationale to lithologies from other sites should be done with caution since Rades et al. (2018) have previously applied L_{nat}/L_{sat} ratio correction with success. When comparing both methods in their study, they received indistinguishable ages between g-value correction and L_{nat}/L_{sat} ratio for one boulder. For a second boulder, however, only the L_{nat}/L_{sat} ratio yielded a realistic age. The most appropriate fading correction approach could therefore vary between different lithologies, or be dependent on the size of the burial dose which is to be corrected; the latter since fading rates are expected to be higher for larger doses (Huntley and Lian, 2006). Rades et al. (2018) discussed that the L_{nat}/L_{sat} ratio represents an upper limit for fading estimates. If so, the L_{nat}/L_{sat} approach may be more suitable to older samples with luminescence intensities closer to saturation, compared to the Huntley and Lamothe (2001) approach which is more reliable in the lower dose range.

6.3. Chronostratigraphy

The burial age of ∽19 ka derived from cobble MZ051S-8 is clearly not associated with the occupation of MZ051S, but rather dates a

burial event during the glaciation/deglaciation cycles in the Upper Pleistocene. Radiocarbon dating of soil organic matter and ^{10}Be cosmogenic nuclide dating from the adjacent Val di Rabbi shows cycles of ice retreat and advances which started ∽18 ka cal. BP (Favilli et al., 2009). It is, therefore, possible that MZ051S-8 would have been exposed and subsequently buried during the early phase of deglaciation. More samples, preferably from primary depositions, are needed to verify such an event. We also cannot exclude that erosion has removed the more recent exposure history of the cobble. Charcoal fragments from Alpine soils (1800–2200 m above sea level) in Val di Sole have been dated to the early Holocene (∽8900–8200 BC), which is a clear indication that at this time, the area was deglaciated and post-glacial soil formation had begun (Favilli et al., 2010). Soil formation in the Early Holocene has been confirmed by radiocarbon dating of charcoal (∽6550–6450 cal. BC) from the adjacent tributary valley of Val Molinac, and slightly later (∽4600–4500 and ∽4800–4700 cal. BC) also in Val Poré (Angelucci and Carrer, 2015). It is, therefore, well-established that the landscape in Val Poré remained relatively stable during the early and middle Holocene, which would have enabled soil formation (Fig. 11.1).

The previously reported, first known human occupation in Val Poré, dated to 1880–1691 BC (Angelucci et al., 2017), is confirmed by the new radiocarbon ages (COL6512.1.1: ∽1750–1450 BC; COL6513.1.1: ∽2100–1750 BC) from unit US5a at MZ051S (Fig. 11.2). These ages (together with radiocarbon age DSH6955 and the archaeological evidence) demonstrate that human groups occupied the Holocene topsoil during the Early Bronze Age. The occupied surface was subsequently buried by colluvium, deposited during a short period of reactivation of slope dynamics due to geomorphological instability (Fig. 11.3). The timing of such activities and the subsequent formation of US4a is currently not fully constrained. The previously published radiocarbon age DSH6956 (∽1550–1450 cal. BC) from US4a pinpoints the occurrence of human activities in the area during the Middle Bronze Age (Angelucci et al., 2017) and the possible reoccupation of MZ051S during this period. Logically, the top surface of cobble MZ051S-7 (collected from US5a) should represent the burial of US5a, i.e. the onset of deposition of colluvium, and should therefore pre-date US4a. However, the burial age (1460–720 BC) of MZ051S-7 is slightly younger than DSH6956 at 1σ. This chronological inconsistency is not yet resolved. Although the reworking of sample DSH6956 from US5a is a possibility (which could result in age overestimation), the stratigraphic evidence suggests that the top surface of MZ051S-7 was exposed even after the deposition of the colluvium superimposing US5a. It is, therefore, our current interpretation that MZ051S-7 slightly underestimates the burial age of US5a. We consider the likeliest explanation for this to be the continued exposure of the top surface of MZ051S-7, even after the deposition of colluvium. The thinning of colluvium further away from the slope (where MZ051S-7 was collected) suggests that the explanation of a slightly protruding top surface of MZ051S-7 is quite likely. Additional age estimates from cobbles from US5a, combined with detailed observation of the vertical position of their top surface, could in the future help to establish the time of burial of US5a with more confidence; a re-interpretation of the onset of slope activities and the chronostratigraphic implication for MZ051S-7 might then be necessary.

Our dating efforts indicate that US4a remained exposed for a considerable time (Fig. 11.4), perhaps more than a millennium, before the reactivation of the nearby slope (Fig. 11.5). The heating event exhibited in MZ051S-2 provides a minimum age for the formation of unit US4a, together with the first date for human reoccupation at or near MZ051S. While the large dating uncertainty of this event prevents precise pinpointing for chronostratigraphic purposes, we now know, despite the scarcity of archaeological finds from US4a, that some human activity likely occurred at MZ051S during the Late Bronze Age or the Iron Age. Traces of human occupation (potsherds) in Val Poré from these periods have previously been discovered at the nearby dry-stone enclosure named MZ005S (Angelucci and Carrer, 2015). The new radiocarbon ages COL6511.1.1 and COL6514.1.1 from US4a show that the surface of US4a remained exposed and stable, at least until the 5th–7th centuries AD. This observation is confirmed by burial ages from MZ051S-3 and the top of MZ051S-2, albeit that these cobble ages (except the top of MZ051S-3) suggest a slightly later time of burial at ∽AD 1000. These age disparities are small when dating uncertainties are considered, but an explanation for the observed scatter between the methods could be that they do not date the same event. While the radiocarbon ages date the death of trees from which wood was subsequently burned (both events could have occurred long before the final burial of US4a), the cobbles date the end of the last exposure of US4a. Therefore, our interpretation is that human activity occurred at or near MZ051S in the Early Middle Ages (dated by radiocarbon), which was followed by the initiation of the second period of slope instability (possibly due to human land use) towards the end of the 1st millennium AD/beginning of the 2nd millennium AD (constrained by cobble dating). Slope instability in Val Poré continued to occur during the 2nd millennium AD, as was previously confirmed during the excavation of MZ005S. At this site, at least two generations of colluvium are recorded. These have sealed an ephemeral surface dating from the 7th–8th centuries AD, and the early-Modern artefact-bearing topsoil (Carrer and Angelucci, 2013). At MZ051S, present soil formation was initiated following the deposition of colluvium (Fig. 11.6).

7. Conclusions

The investigated rock surfaces from MZ051S in Val di Sole display various levels of resetting before burial, a prerequisite for burial dating. The presented research aimed to examine the suitability of rock surface IRSL to date buried dry-stone structures linked to pastoralism in upland pastures. Our first results from Val di Sole show encouraging signs for the applicability of the method to such, from a dating point of view, challenging archaeological structures. We here provide new information on the chronostratigraphic development of the livestock enclosure MZ051S in the Italian Alps. Combined rock surface IRSL dating and radiocarbon dating show that the upper archaeological unit US4a was exposed from the Bronze Age until the Middle Ages, perhaps as late as at the shift between the 1st and 2nd millennia AD. The agreement shows the potential of rock surface IRSL dating as a chronological tool to date buried stone structures and to corroborate radiocarbon dating in contexts where such dating is challenging. For the lower archaeological unit US5a, the relationship between the cobble ages and the general chronostratigraphy is more complicated and requires further investigations.

One unexpected discovery from our research in Val di Sole is that one cobble demonstrates both optical bleaching and annealing by heat, which had occurred during different events in the past. The timing of such events is recorded within the luminescence-depth profiles; these events can be dated using both $IRSL_{50}$ and pIR-$IRSL_{290}$ dating techniques. A possible explanation for annealing is forest fires, which could occur naturally or induced by humans. None of the other cobbles from our site (including the smaller MZ051S-3) show any signs of resetting in the centre of the cobbles. Thus, we argue that in this case, we can directly date human activities with rock surface IRSL dating. The dating of the heating event demonstrates that the dry-stone structure MZ051S must have been occupied, at least ephemerally, even after the Early Bronze Age. The implication of our observations is that rock surface IRSL dating can be applied at archaeological sites to date heating events, even if no heated artefacts have been recovered. Furthermore, the archaeological implication is that rock surface luminescence dating may help to detect ephemeral events of human activity, which left no relevant archaeological record and could have remained undetected otherwise.

Questions on how to correct for fading of the feldspar signal in rocks remain. Here, we show that for the heated rock of MZ051S-2, the g-value corrected $IRSL_{50}$ age is in agreement with the more stable pIR-$IRSL_{290}$. However, due to the lack of a naturally saturated signal,

we cannot directly compare such ages with L_{nat}/L_{sat} ratio corrected ages. We here favour the application of g-value corrected ages for the cobbles from Val di Sole, but encourage more research to explore the suitability of different fading correction approaches for rocks of different lithologies and with varying burial doses.

Declaration of competing interest

The authors declare that they have no known competing financial interests or personal relationships that could have appeared to influence the work reported in this paper.

Acknowledgements

Dr. Anja Zander, University of Cologne, is thanked for gamma spectrometry measurements. Laura Vezzoni, University of Trento, is thanked for visual inspections of petrographic thin sections. The authors are grateful to Dr. Fabio Cavulli, University of Trento, for helping during fieldwork and for providing photo-plans of the excavations. Lucas Ageby is funded by the Deutsche Forschungsgemeinschaft (DFG, German Research Foundation) — Project number 57444011 - SFB 806 as part of project F2 in CRC 806 — Our Way To Europe. Francesco Carrer's research is funded by the Newcastle University Academic Track programme (NUAcT), UK. Project ALPES is undertaken in the context of a specific agreement between the Department of Humanities of the University of Trento and the Soprintendenza per i Beni Culturali of the autonomous Province of Trento. The project is funded by the University of Trento, Italy and by the Terre Alte programme of the CAI (Italian Alpine Club) and is supported by the Municipality of Mezzana, Italy (Trento). The authors are indebted to the people from Ortisé and Menas for their help, and to all the students and researchers who have participated in fieldwork activities. The work by Eike F. Rades was funded by the German Research Foundation (DFG) in the framework of a Research Fellowship (RA 2836/1-1). Finally, we thank Dr. Michael Meyer and two anonymous reviewers for their helpful feedback and comments, which greatly improved the manuscript.

Appendix A. Supplementary data

Supplementary material related to this article can be found online at https://doi.org/10.1016/j.quageo.2021.101212.

References

Aitken, M.J., 1985. Thermoluminescence Dating. Academic Press, London.

al Khasawneh, S., Murray, A., Abudanah, F., 2019. A first radiometric chronology for the Khatt Shebib megalithic structure in Jordan using the luminescence dating of rock surfaces. Quat. Geochronol. 49, 205–210. http://dx.doi.org/10.1016/j.quageo.2018.02.007.

al Khasawneh, S., Murray, A., Bonatz, D., Freiesleben, T., 2015. Testing the application of post IR IRSL dating to Iron- and Viking-age ceramics and heated stones from Denmark. Quat. Geochronol. 30, 386–391. http://dx.doi.org/10.1016/j.quageo.2015.05.014.

Angelucci, D.E., Anesin, D., 2012. Sedimenti e suoli, natura e cultura. Considerazioni geoarcheologiche sulla genesi delle stratificazioni archeologiche in ambiente montano. In: APSAT 1. Teoria E Metodi Della Ricerca Sui Paesaggi D'Altura, Mantova. SAP Società Archeologica, Mantova, pp. 11–25.

Angelucci, D.E., Carrer, F., 2015. Paesaggi Pastorali Dalta Quota in Val Di Sole (Trento): Le Ricerche Del Progetto ALPES, 2010-2014. Universita degli studi di Trento, Dipartimento di Lettere Filosofia.

Angelucci, D.E., Carrer, F., Cavulli, F., 2014. Shaping a periglacial land into a pastoral landscape: a case study from Val di Sole (Trento, Italy). Post-Class. Archaeol. 4 (2014), 157–180.

Angelucci, D.E., Carrer, F., Pedrotti, A., 2017. Due nuove datazioni dell'età del Bronzo da un Sito D'alta quota in Val Poré (Val di Sole). In: Archeologia Delle Alpi. Provincia autonoma di Trento, pp. 154–156.

Auclair, M., Lamothe, M., Huot, S., 2003. Measurement of anomalous fading for feldspar IRSL using SAR. Radiat. Meas. 37 (4), 487–492. http://dx.doi.org/10.1016/S1350-4487(03)00018-0.

Bøtter-Jensen, L., Thomsen, K., Jain, M., 2010. Review of optically stimulated luminescence (OSL) instrumental developments for retrospective dosimetry. Radiat. Meas. 45 (3), 253–257. http://dx.doi.org/10.1016/j.radmeas.2009.11.030.

Brodard, A., Guibert, P., cois Lévêque, F., Mathé, V., Carozza, L., Burens, A., 2012. Thermal characterization of ancient hearths from the cave of Les Fraux (Dordogne, France) by thermoluminescence and magnetic susceptibility measurements. Quat. Geochronol. 10, 353–358. http://dx.doi.org/10.1016/j.quageo.2012.04.013.

Bronk Ramsey, C., 2009. Bayesian Analysis of radiocarbon dates. Radiocarbon 51 (1), 337–360. http://dx.doi.org/10.1017/S0033822200033865.

Burow, C., 2019. calc_ CosmicDoseRate: Calculate the cosmic dose rate. function version 0.5.2. In: Kreutzer, S., Burow, C., Dietze, M., Fuchs, M., Schmidt, C., Fischer, M., Friedrich, J. (Eds.), Luminescence: Comprehensive Luminescence Dating Data Analysis. R Package Version 0.9.0.109.

Buylaert, J.-P., Jain, M., Murray, A.S., Thomsen, K.J., Thiel, C., Sohbati, R., 2012. A robust feldspar luminescence dating method for Middle and Late Pleistocene sediments. Boreas 41 (3), 435–451. http://dx.doi.org/10.1111/j.1502-3885.2012.00248.x.

Carcaillet, C., 2001. Are Holocene wood-charcoal fragments stratified in alpine and subalpine soils? Evidence from the Alps based on AMS^{14}C dates. Holocene 11 (2), 231–242. http://dx.doi.org/10.1191/095968301674071040.

Carrer, F., 2012. Upland sites and pastoral landscapes. New perspectives into the archaeology of pastoralism in the Alps. In: Brogiolo, G., Angelucci, D., Colecchia, A., Remondino, F. (Eds.), APSAT 1. Teoria E Metodi Della Ricerca Sui Paesaggi D'Altura, Mantova. SAP Società Archeologica, Mantova, pp. 101–116.

Carrer, F., Angelucci, D.E., 2013. First archaeological data from an Alpine pastoral enclosure at Val Porè (Val Di Sole, Trentino, Italy). Debates de Arqueología Mediveal 3 (2013), 149–165.

Carrer, F., Angelucci, D.E., 2018. Continuity and discontinuity in the history of upland pastoral landscapes: the case study of Val Molinac and Val Porè (Val di Sole, Trentino, Eastern Italian alps). Landscape Res. 43 (6), 862–877. http://dx.doi.org/10.1080/01426397.2017.1390078.

Carrer, F., Colonese, A.C., Lucquin, A., Petersen Guedes, E., Thompson, A., Walsh, K., Reitmaier, T., Craig, O.E., 2016. Chemical analysis of pottery demonstrates prehistoric origin for high-altitude alpine dairying. PLoS One 11 (4), e0151442. http://dx.doi.org/10.1371/journal.pone.0151442.

Cavulli, F., Grimaldi, S., Pedrotti, A., Angelucci, D.E., 2011. Toward an understanding of archaeological visibility: the case of the Trentino (southern Alps). In: van Leusen, M., Pizziolo, G., Sarti, L. (Eds.), Hidden Landscapes of Mediterranean Europe. Cultural and Methodological Biases in Pre- and Protohistoric Landscape Studies. Proceedings of the International Meeting, Siena, Italy, May 25-27, 2007. BAR International Series 2320, pp. 83–94.

Colarossi, D., Duller, G., Roberts, H., 2018. Exploring the behaviour of luminescence signals from feldspars: Implications for the single aliquot regenerative dose protocol. Radiat. Meas. 109, 35–44. http://dx.doi.org/10.1016/j.radmeas.2017.07.005.

Cresswell, A., Carter, J., Sanderson, D., 2018. Dose rate conversion parameters: Assessment of nuclear data. Radiat. Meas. 120, 195–201. http://dx.doi.org/10.1016/j.radmeas.2018.02.007.

Dal Piaz, G., Castellarin, A., Martin, S., Selli, L., Carton, A., Pellegrini, G., Casolari, E., Daminato, F., Montresor, L., Picotti, V., Prosser, G., Santuliana, E., Cantelly, L., 2007. Carta Geologica d'Italia alla scala 1:50.000. Foglio 042. Malé + Note illustrative della Carta Geologica d'Italia alla scala 1:50.000. Trento-Roma.

Dell'Amore, F., Carrer, F., Angelucci, D.E., 2017. Reperti archeologici dalla Val Molinac e dalla Val Poré (Val di Sole, Trento, Italia). Atti Del Convegno Archeologia E Cultura in Val Di Sole: Ricerche, Contesti, Prospettive. pp. 131–143.

Dewald, A., Heinze, S., Jolie, J., Zilges, A., Dunai, T., Rethemeyer, J., Melles, M., Staubwasser, M., Kuczewski, B., Richter, J., Radtke, U., von Blanckenburg, F., Klein, M., 2013. CologneAMS, a dedicated center for accelerator mass spectrometry in Germany. Nucl. Instrum. Methods Phys. Res. B 294, 18–23. http://dx.doi.org/10.1016/j.nimb.2012.04.030.

Duller, G.A., 2015. The analyst software package for luminescence data: overview and recent improvements. Ancient TL 33 (1), 35–42.

Favilli, F., Cherubini, P., Collenberg, M., Egli, M., Sartori, G., Schoch, W., Haeberli, W., 2010. Charcoal fragments of Alpine soils as an indicator of landscape evolution during the Holocene in Val di Sole (Trentino, Italy). Holocene 20 (1), 67–79. http://dx.doi.org/10.1177/0959683609348850.

Favilli, F., Egli, M., Brandova, D., Ivy-Ochs, S., Kubik, P.W., Maisch, M., Cherubini, P., Haeberli, W., 2009. Combination of numerical dating techniques using^{10}Be in rock boulders and^{14}C of resilient soil organic matter for reconstructing the chronology of glacial and periglacial processes in a high Alpine catchment during the Late Pleistocene and Early Holocene. Radiocarbon 51 (2), 537–552. http://dx.doi.org/10.1017/S0033822200055910.

Feathers, J., More, G.M., Quinteros, P.S., Burkholder, J.E., 2019. IRSL Dating of rocks and sediments from desert geoglyphs in coastal peru. Quat. Geochronol. 49, 177–183. http://dx.doi.org/10.1016/j.quageo.2018.07.009.

Festi, D., Putzer, A., Oeggl, K., 2014. Mid and late Holocene land-use changes in the Ötztal Alps, territory of the Neolithic Iceman "Ötzi". Quat. Int. 353, 17–33. http://dx.doi.org/10.1016/j.quaint.2013.07.052.

Flude, S., Haschke, M., Storey, M., 2017. Application of benchtop micro-XRF to geological materials. Mineral. Mag. 81 (4), 923–948. http://dx.doi.org/10.1180/minmag.2016.080.150.

Freiesleben, T., Sohbati, R., Murray, A., Jain, M., al Khasawneh, S., Hvidt, S., Jakobsen, B., 2015. Mathematical model quantifies multiple daylight exposure and burial events for rock surfaces using luminescence dating. Radiat. Meas. 81, 16–22. http://dx.doi.org/10.1016/j.radmeas.2015.02.004.

Fuchs, M., Lang, A., 2009. Luminescence dating of hillslope deposits—-A review. Geomorphology 109 (1), 17–26. http://dx.doi.org/10.1016/j.geomorph.2008.08.025.

Galli, A., Panzeri, L., Rondini, P., Poggiani Keller, R., Martini, M., 2020. Luminescence dating of rock surface. The case of monoliths from the megalithic sanctuary of Ossimo-Pat (Valle Camonica, Italy). Appl. Sci. 10, 7403. http://dx.doi.org/10.3390/app10217403.

Gliganic, L., Meyer, M., Sohbati, R., Jain, M., Barrett, S., 2019. OSL Surface exposure dating of a lithic quarry in Tibet: Laboratory validation and application. Quat. Geochronol. 49, 199–204. http://dx.doi.org/10.1016/j.quageo.2018.04.012.

Habermann, J., Schilles, T., Kalchgruber, R., Wagner, G.A., 2000. Steps towards surface dating using luminescence. Radiat. Meas. 32 (5), 847–851. http://dx.doi.org/10.1016/S1350-4487(00)00066-4.

Hafner, A., Schwörer, C., 2018. Vertical mobility around the high-alpine Schnidejoch Pass. Indications of Neolithic and Bronze Age pastoralism in the Swiss Alps from paleoecological and archaeological sources. Quat. Int. 484, 3–18. http://dx.doi.org/10.1016/j.quaint.2016.12.049.

Huntley, D.J., Baril, M., 1997. The K content of the K-feldspars being measured in optical dating or in thermoluminescence dating. Ancient TL 15 (1), 11–13.

Huntley, D.J., Lamothe, M., 2001. Ubiquity of anomalous fading in K-feldspars and the measurement and correction for it in optical dating. Can. J. Earth Sci. 38 (7), 1093–1106. http://dx.doi.org/10.1139/e01-013.

Huntley, D., Lian, O.B., 2006. Some observations on tunnelling of trapped electrons in feldspars and their implications for optical dating. Quat. Sci. Rev. 25 (19), 2503–2512. http://dx.doi.org/10.1016/j.quascirev.2005.05.011.

Junge, A., Lomax, J., Shahack-Gross, R., Dunseth, Z.C., Finkelstein, I., Fuchs, M., 2016. OSL Age determination of archaeological stone structures using trapped aeolian sediments: A case study from the negev highlands, Israel. Geoarchaeology 31 (6), 550–563. http://dx.doi.org/10.1002/gea.21578.

Kars, R.H., Reimann, T., Ankjærgaard, C., Wallinga, J., 2014. Bleaching of the post-IR IRSL signal: new insights for feldspar luminescence dating. Boreas 43 (4), 780–791. http://dx.doi.org/10.1111/bor.12082.

Klasen, N., Kehl, M., Mikdad, A., Brückner, H., Weniger, G.-C., 2018. Chronology and formation processes of the Middle to Upper Palaeolithic deposits of Ifri n'Ammar using multi-method luminescence dating and micromorphology. Quat. Int. 485, 89–102. http://dx.doi.org/10.1016/j.quaint.2017.10.043.

Kothieringer, K., Walser, C., Dietre, B., Reitmaier, T., Haas, J.N., Lambers, K., 2015. High impact: early pastoralism and environmental change during the Neolithic and Bronze Age in the Silvretta Alps (Switzerland/Austria) as evidenced by archaeological, palaeoecological and pedological proxies. Z. Geomorphol. Suppl. Issue 59 (2), 177–198. http://dx.doi.org/10.1127/zfg_suppl/2015/S-59210.

Kreutzer, S., 2020. calc_ FadingCorr: Apply a fading correction according to Huntley & Lamothe (2001) for a given g-value and a given tc. Function version 0.4.2. In: Kreutzer, S., Burow, C., Dietze, M., Fuchs, M., Schmidt, C., Fischer, M., Friedrich, J., Riedesel, S., Autzen, M., Mittelstrass, D. (Eds.), Luminescence: Comprehensive Luminescence Dating Data Analysis. R Package Version 0.9.0.10.

Kreutzer, S., Burow, C., 2020. analyse_ FadingMeasurement: Calculate the cosmic dose rate. Function version 0.1.15. In: Kreutzer, S., Burow, C., Dietze, M., Fuchs, M., Schmidt, C., Fischer, M., Friedrich, J., Riedesel, S., Autzen, M., Mittelstrass, D. (Eds.), Luminescence: Comprehensive Luminescence Dating Data Analysis. R Package Version 0.9.0.10.

Lehmann, B., Herman, F., Valla, P.G., King, G.E., Biswas, R.H., Ivy-Ochs, S., Steinemann, O., Christl, M., 2020. Postglacial erosion of bedrock surfaces and deglaciation timing: New insights from the Mont Blanc massif (western Alps). Geology 48 (2), 139–144. http://dx.doi.org/10.1130/G46585.1.

Leveau, P., Walsh, K., 2005. Population sequences in a high altitude alpine environment: Archaeological sites and historical and environmental time. Int. J. Anthropol. 20 (3), 155–171. http://dx.doi.org/10.1007/BF02443056.

Li, B., Li, S.-H., 2011a. Luminescence dating of K-feldspar from sediments: A protocol without anomalous fading correction. Quat. Geochronol. 6 (5), 468–479. http://dx.doi.org/10.1016/j.quageo.2011.05.001.

Li, B., Li, S.-H., 2011b. Thermal stability of infrared stimulated luminescence of sedimentary K-feldspar. Radiat. Meas. 46 (1), 29–36. http://dx.doi.org/10.1016/j.radmeas.2010.10.002.

Medici, T., Foradori, G., Carrer, F., Dal Maschio, R., Gialanella, S., Montagna, M., Pedrotti, A., Angelucci, D.E., 2014. Una perlina in vetro da un contesto pastorale dalta quota della Val di Sole (Trento). In: Ciappi, S., Larese, A., Uboldi, M. (Eds.), Il Vetro in Età Protostorica in Italia, Atti Delle XVI Giornate Nazionali Di Studio Sul Vetro (Adria, 12-13 Maggio 2012). Comitato Nazionale Italiano AIHV (Association Internationale pour l'Histoire du Verre), Venezia, pp. 115–121.

Meyer, M., Gliganic, L., Jain, M., Sohbati, R., Schmidmair, D., 2018. Lithological controls on light penetration into rock surfaces — Implications for OSL and IRSL surface exposure dating. Radiat. Meas. 120, 298–304. http://dx.doi.org/10.1016/j.radmeas.2018.03.004.

Moe, D., Fedele, F.G., Maude, A.E., Kvamme, M., 2007. Vegetational changes and human presence in the low-alpine and subalpine zone in Val Febbraro, upper Valle di Spluga (Italian central Alps), from the Neolithic to the Roman period. Veg. Hist. Archaeobot. 16 (6), 431–451. http://dx.doi.org/10.1007/s00334-006-0088-0.

Murray, A., Buylaert, J., Thomsen, K., Jain, M., 2009. The effect of preheating on the IRSL signal from feldspar. Radiat. Meas. 44 (5), 554–559. http://dx.doi.org/10.1016/j.radmeas.2009.02.004.

Murray, A., Schmidt, E., Stevens, T., Buylaert, J.-P., Marković, S., Tsukamoto, S., Frechen, M., 2014. Dating Middle Pleistocene loess from Stari Slankamen (Vojvodina, Serbia) —- limitations imposed by the saturation behaviour of an elevated temperature IRSL signal. CATENA 117, 34–42. http://dx.doi.org/10.1016/j.catena.2013.06.029.

Murray, A., Wintle, A., 2000. Luminescence dating of quartz using an improved single-aliquot regenerative-dose protocol. Radiat. Meas. 32 (1), 57–73. http://dx.doi.org/10.1016/S1350-4487(99)00253-X.

Ou, X., Roberts, H., Duller, G., Gunn, M., Perkins, W., 2018. Attenuation of light in different rock types and implications for rock surface luminescence dating. Radiat. Meas. 120, 305–311. http://dx.doi.org/10.1016/j.radmeas.2018.06.027.

Prescott, J., Hutton, J., 1988. Cosmic ray and gamma ray dosimetry for TL and ESR. Int. J. Radiat. Appl. Instrum. D 14 (1), 223–227. http://dx.doi.org/10.1016/1359-0189(88)90069-6.

Prescott, J., Stephan, L., 1982. The contribution of cosmic radiation to the environmental dose for thermoluminescence dating. Latitude, altitude and depth dependences. Pact 6, 17–25.

R. Core Team, 2019. R: A Language and Environment for Statistical Computing. R Foundation for Statistical Computing, Vienna, Austria.

Rades, E., Sohbati, R., Lüthgens, C., Jain, M., Murray, A., 2018. First luminescence-depth profiles from boulders from moraine deposits: Insights into glaciation chronology and transport dynamics in Malta valley, Austria. Radiat. Meas. 120, 281–289. http://dx.doi.org/10.1016/j.radmeas.2018.08.011.

Reimer, P.J., Austin, W.E.N., Bard, E., Bayliss, A., Blackwell, P.G., Bronk Ramsey, C., Butzin, M., Cheng, H., Edwards, R.L., Friedrich, M., et al., 2020. The IntCal20 northern hemisphere radiocarbon age calibration curve (0–55 cal kBP). Radiocarbon 62 (4), 725–757. http://dx.doi.org/10.1017/RDC.2020.41.

Reitmaier, T., Doppler, T., Pike, A.W., Deschler-Erb, S., Hajdas, I., Walser, C., Gerling, C., 2018. Alpine cattle management during the Bronze Age at Ramosch-Mottata, Switzerland. Quat. Int. 484, 19–31. http://dx.doi.org/10.1016/j.quaint.2017.02.007.

Rethemeyer, J., Gierga, M., Heinze, S., Stolz, A., Wotte, A., Wischhöfer, P., Berg, S., Melchert, J., Dewald, A., 2019. Current sample preparation and analytical capabilities of the Radiocarbon Laboratory at CologneAMS. Radiocarbon 61 (5), 1449–1460. http://dx.doi.org/10.1017/RDC.2019.16.

Riedesel, S., Brill, D., Roberts, H.M., Duller, G.A., Garrett, E., Zander, A.M., King, G.E., Tamura, T., Burow, C., Cunningham, A., Seeliger, M., Batist, M.D., Heyvaert, V.M., Fujiwara, O., Brückner, H., 2018. Single-grain feldspar luminescence chronology of historical extreme wave event deposits recorded in a coastal lowland, Pacific coast of central Japan. Quat. Geochronol. 45, 37–49. http://dx.doi.org/10.1016/j.quageo.2018.01.006.

Schiffer, M.B., 1986. Radiocarbon dating and the "old wood" problem: The case of the Hohokam chronology. J. Archaeol. Sci. 13 (1), 13–30. http://dx.doi.org/10.1016/0305-4403(86)90024-5.

Sohbati, R., Jain, M., Murray, A., 2012c. Surface exposure dating of non-terrestrial bodies using optically stimulated luminescence: A new method. Icarus 221 (1), 160–166. http://dx.doi.org/10.1016/j.icarus.2012.07.017.

Sohbati, R., Liu, J., Jain, M., Murray, A., Egholm, D., Paris, R., Guralnik, B., 2018. Centennial- to millennial-scale hard rock erosion rates deduced from luminescence-depth profiles. Earth Planet. Sci. Lett. 493, 218–230. http://dx.doi.org/10.1016/j.epsl.2018.04.017.

Sohbati, R., Murray, A.S., Buylaert, J.-P., Almeida, N.A.C., Cunha, P.P., 2012a. Optically stimulated luminescence (OSL) dating of quartzite cobbles from the Tapada do Montinho archaeological site (east-central Portugal). Boreas 41 (3), 452–462. http://dx.doi.org/10.1111/j.1502-3885.2012.00249.x.

Sohbati, R., Murray, A.S., Chapot, M.S., Jain, M., Pederson, J., 2012b. Optically stimulated luminescence (OSL) as a chronometer for surface exposure dating. J. Geophys. Res.: Solid Earth 117 (B9), http://dx.doi.org/10.1029/2012JB009383.

Sohbati, R., Murray, A., Jain, M., Buylaert, J.-P., Thomsen, K., 2011. Investigating the resetting of OSL signals in rock surfaces. Geochronometria 38 (3), http://dx.doi.org/10.2478/s13386-011-0029-2.

Sohbati, R., Murray, A., Jain, M., Thomsen, K., Hong, S.-C., Yi, K., Choi, J.-H., 2013. Na-rich feldspar as a luminescence dosimeter in infrared stimulated luminescence (IRSL) dating. Radiat. Meas. 51–52, 67–82. http://dx.doi.org/10.1016/j.radmeas.2012.12.011.

Sohbati, R., Murray, A., Porat, N., Jain, M., Avner, U., 2015. Age of a prehistoric "Rodedian" cult site constrained by sediment and rock surface luminescence dating techniques. Quat. Geochronol. 30, 90–99. http://dx.doi.org/10.1016/j.quageo.2015.09.002.

Spooner, N., 1994. The anomalous fading of infrared-stimulated luminescence from feldspars. Radiat. Meas. 23 (2), 625–632. http://dx.doi.org/10.1016/1350-4487(94)90111-2.

Thomsen, K., Murray, A., Jain, M., 2011. Stability of IRSL signals from sedimentary K-feldspar samples. Geochronometrica 38 (1), 1–13. http://dx.doi.org/10.2478/s13386-011-0003-z.

Thomsen, K., Murray, A., Jain, M., Bøtter-Jensen, L., 2008. Laboratory fading rates of various luminescence signals from feldspar-rich sediment extracts. Radiat. Meas. 43 (9), 1474–1486. http://dx.doi.org/10.1016/j.radmeas.2008.06.002.

Vafiadou, A., Murray, A., Liritzis, I., 2007. Optically stimulated luminescence (OSL) dating investigations of rock and underlying soil from three case studies. J. Archaeol. Sci. 34 (10), 1659–1669. http://dx.doi.org/10.1016/j.jas.2006.12.004.

Walsh, K., Court-Picon, M., de Beaulieu, J.-L., Guiter, F., Mocci, F., Richer, S., Sinet, R., Talon, B., Tzortzis, S., 2014. A historical ecology of the ecrins (Southern French Alps): Archaeology and palaeoecology of the Mesolithic to the Medieval period. Quat. Int. 353, 52–73. http://dx.doi.org/10.1016/j.quaint.2013.08.060.

Walsh, K., Mocci, F., 2011. Mobility in the mountains: Late third and second millennia alpine societies' engagements with the high-altitude zones in the Southern French Alps. Eur. J. Archaeol. 14 (1–2), 88–115. http://dx.doi.org/10.1179/146195711798369427.

Walsh, K., Mocci, F., Palet-Martinez, J., 2007. Nine thousand years of human/landscape dynamics in a high altitude zone in the southern French Alps (Parc National des Ecrins, Hautes-Alpes). Preistoria Alp. 42, 9–22.

Wintle, A., 1977. Detailed study of a thermoluminescent mineral exhibiting anomalous fading. J. Lumin. 15 (4), 385–393. http://dx.doi.org/10.1016/0022-2313(77)90037-0.

Zander, A., Strebler, D., Classen, E., Rethemeyer, J., Brückner, H., 2019. Roman traces in Germania magna: New thermoluminescence and $pIRIR_{290}$ data from a lime kiln at Bergisch Gladbach, Germany. Archaeometry 61 (2), 506–518. http://dx.doi.org/10.1111/arcm.12435.